Lunds Tekniska Högskola

Master's Thesis

Fast Photoneutron Detection

Author:
Emil Rofors

Supervisor:
Kevin Fissum

A thesis submitted in fulfilment of the requirements for the degree of Master of Science

in the

Department of Physics
Division of Nuclear Physics

March 2016

Lunds universitet
Lunds Tekniska Högskola

LUND UNIVERSITEY

Abstract

Physics Depatement
Division of Nuclear Physics

Master of Science

Fast Photoneutron Detection

by Emil Rofors

The purpose of this project was to investigate fast photoneutron production from a series of materials commonly used for backing neutron beam guides. Fast neutrons were knocked out of these materials by exposing them to to high-energy photons at the Tagged-Photon Facility at MAX-lab in Lund, Sweden. Liquid scintillator detectors at different angles around the targets registered the photoknockout neutrons. These fast-neutron detectors were energy calibrated using two well-understood gamma-ray sources. The energy calibrations were used to establish the hardware detector thresholds. The hardware thresholds server as input to an absolute neutron-detection efficiency Monte Carlo simulation known as STANTON, which was used to establish the best-case neutron-detection efficiency achieved in the measurement. Finally, the detector thresholds were increased in software to study the reduction in detection efficiency as a function of the increase in threshold. A complete overview of the project is presented.

Acknowledgements

During this work I have gotten to work with many helpful, very nice persons.

I would like to thank Irina Stefanescu of the ESS Detector Group for your guidance and explanations during the ^{10}B detector project. From the Neutron Optics and Shielding Group of ESS, thanks to Douglas Di Julio and Carsten Cooper-Jensen. Thank you John Annand and Ramsey Al Jebali of University of Glasgow. Many thanks also to Julius Scherzinger and Hanno Perrey of the nuclear department at Lund University. For the assistance by explanations, writing comments and other help, thank you Kevin Fissum, the supervisor of this master thesis.

Contents

List of Figures

List of Tables

Abbreviations

CFD	**C**onstant **F**raction **D**iscriminator
CW	**C**ontinous **W**ave
Δ	Delta resonance
ee	**e**lectron **e**quivalent
GDR	**G**iant **D**ipole **R**egion
INT	**INT**erupt
MCA	**M**ulti-**C**hannel **A**nalyzer
PMT	**P**hoto-**M**ultiplier **T**ube
STF	**S**ource-**T**esting **F**acility
TDC	**T**ime-to-**D**igtal **C**onverter
QDC	Charge(**Q**)-to-**D**igital **C**onverter

Chapter 1

Introduction

1.1 The neutron

Ernest Rutherford became known as the father of nuclear physics for his discoveries. His model of the atom as a heavy positively charged center with light, negative charges orbiting around it was first proposed in 1911. But he knew already then that something was missing in the model as the mass of the positive protons was not enough to counter the electrostatic repulsion they would exert on each other to allow them to remain so close to one another. There had to be something more. In 1920, the "something more" was put forth when he proposed the existence of the neutrally charged "neutron". The existence of the neutron was established by his associate James Chadwick in 1932, who recognized that it was in fact the unknown penetrating radiation that Walther Böthe and Herbert Becker had already discovered in 1930, when bombarding beryllium plates with alpha particles. The neutron was shown to have about the same mass as the proton but no charge. By the mid 1960's, physicists realized that protons and neutrons themselves were not fundamental particles, but instead each consisted of three up-quarks or down-quarks, see Fig. 1.1.

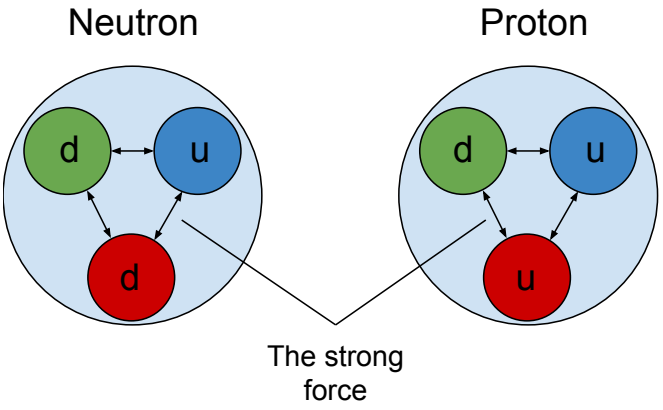

FIGURE 1.1: The quark structure of a neutron and a proton. "u" represents an "up" quark, and "d" represents a "down" quark.

The quarks are held together by the strong force — a force that attracts all nucleons once separated by about 1 fm[1]. The balance between this strong force and the repulsive Coulomb force between the protons alone determines if a nucleus is stable or not. Every different combination of protons and neutrons is known as an isotope. The stable isotopes that exist are shown as a stability line in Fig. 1.2.

Neutrons bound in nuclei are stable. A neutron that is not bound in a nucleus is called a free neutron. Free neutrons have a mean lifetime of about 15 minutes [2]. Free neutrons β-decay into a proton and an electron according to

$$n \rightarrow p + e^{-} + \overline{v}_e, \tag{1.1}$$

where n is the neutron, p is a proton, e^{-} is an electron, and $\overline{v}_e$ is an electron-associated antineutrino. There is a net loss of mass from the initial to the final state. This difference is called the Q-value of the process, 0.782 ± 0.013 MeV. The Q-value is shared as kinetic energy among the final-state particles.

Because free neutrons lack charge, they penetrate materials well. They only slow down or stop when colliding with a nucleus. This is a property that has been used for imaging, diagnostics, homeland security and more. There are many methods used to free neutrons for these purposes. Cosmic rays naturally free neutrons in the upper atmosphere. Nuclear reactors free neutrons via fission. Fusion reactors also free neutrons. Radioactive sources, both natural and manmade, can free neutrons. The European Spallation Source, ESS, being built in Lund, Sweden, is an accelerator-based neutron source, where the process of spallation will be used to free neutrons for materials-science research.

[1] 1 fm = 10^{-15}m.

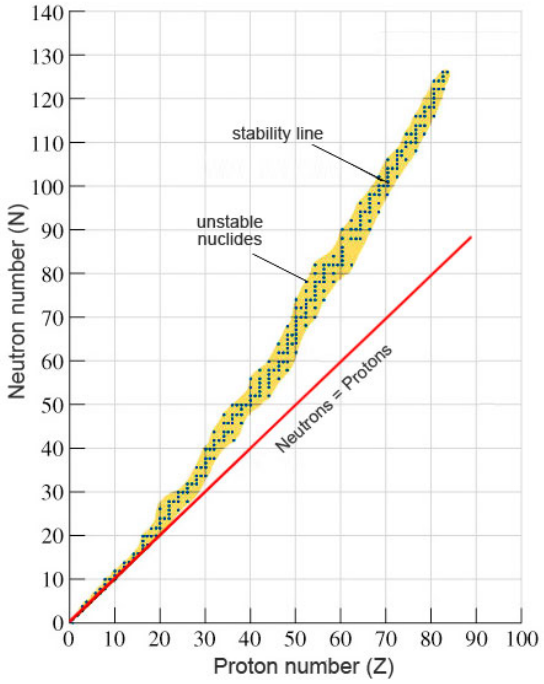

FIGURE 1.2: A plot of number of neutrons against protons for all isotopes. Stable atoms are marked with a dot and the surrounding yellow cloud marks unstable isotopes. Apart from a few of the lightest atoms, all the isotopes have more neutrons than protons. Figure from Ref. [1].

1.2 Spallation

Spallation may be envisioned by considering the balls on a billiard table. In billiards, the cue ball is used to strike the rack of colored balls, breaking apart the stable triangular lattice and setting them individually into motion. Let a highly energetic proton be the cue ball and the spallation target be the rack of colored balls. Certain of the colored balls are neutrons, which are freed. The number of neutrons released increases in proportion with the atomic number of the spallation target [3]; that is, the number of balls in the rack. This makes all heavy elements reasonable candidates as spallation targets; however, other properties such as good thermal conductivity, little thermal expansion and low radiotoxicity limit the choices. The heavy metals tungsten, mercury and lead are popular spallation targets.

Protons incident upon a spallation target are generally accelerated to relativistic energies using a linear accelerator. At ESS, the accelerator will be ~600 m long and will deliver 2 GeV protons. The neutrons freed using these high-energy protons are also generally highly energetic, and will need to be slowed down dramatically to be useful for imaging applications. This is because high-energy neutrons are deeply penetrating, and tend to simply pass through matter. At ESS, neutrons with much lower energy are of

interest. Such low-energy neutrons are typically refered to as “cold” (0 — 0.025 eV) and “thermal” (0.025 eV). To reduce the energy of the neutrons, the spallation target must be surrounded by a proton-rich “moderating” material. In this moderating material, neutrons scatter elastically from protons, depositing some energy with each scattering event. At ESS, the moderator will consist basically of liquid hydrogen. As the cold and thermal neutrons exit the moderator they will be guided through ~100 m of neutron beam guides that direct them to experiment target stations, see Fig. 1.3. The neutrons propagate through the beam guides in a fashion similar to light travelling in an optical waveguide.

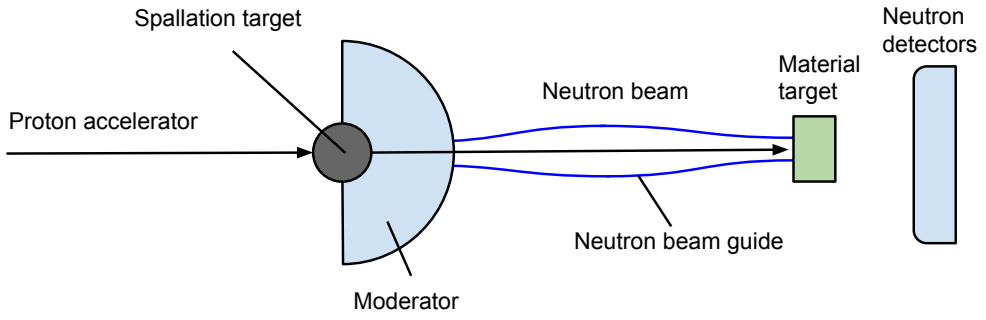

FIGURE 1.3: The principle of a spallation neutron source. High-energy protons hit the spallation target knocking out high-energy neutrons. The moderator slows the high-energy neutrons. They are then directed through neutron beam guides to experiment target stations. At the experiment target stations, the neutrons scatter from targets and are detected in neutron detectors.

Spallation also results in the production of gamma-rays in the spallation target. Nuclear reactions between the neutrons and the moderator, the beam-guide and the shielding can also result in gamma-rays. These gamma-rays can have very high energies, up to hundreds of MeV. Such gamma-rays form a significant background at a spallation source. They can interact with the spallation target, the moderator and the neutron beam guides, producing unwanted backgrounds. One particulary undesirable background at a spallation source is so-called “fast neutrons”, which have energies measured in MeV.

1.3 Photonuclear excitations

Photons with high energies (over ~100 keV) are called gamma-rays. They are ionizing and interact with matter with a certain probability described by the interaction “cross section”. Cross sections are typically reported in the unit barns[2]. A larger cross section means a higher interaction probability. Cross sections depend upon many variables, in particular energy.

[2] 1 barn = 10^{-28} m^2.

Gamma-rays of certain energies interact with matter more easily. The energy range between ~20 — 100 MeV is one such example where the cross section for gamma-ray absorption is unusually large. This energy range is called the "Giant Dipole Resonance" (GDR) region. At ~140 MeV, the threshold for "Pion production" occurs. Above this energy, a nucleon can absorb a gamma-ray and be promoted to its first-excited state. This is called the "Delta-Resonance" (Δ), which peaks at 1232 MeV. The GDR and Δ regions are shown in Fig. 1.4.

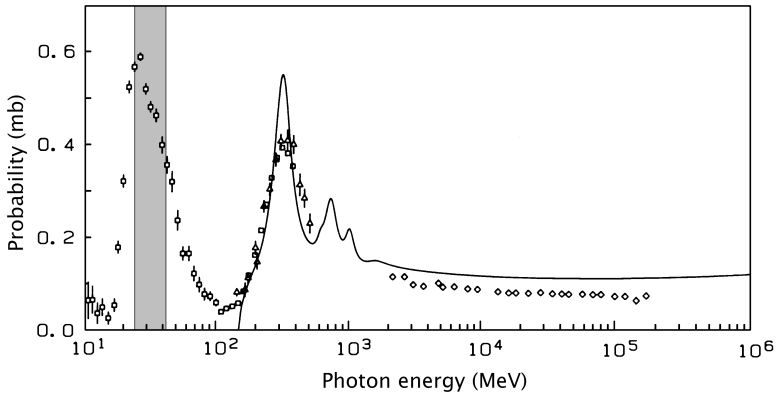

FIGURE 1.4: The GDR region is seen between ~20 — 100 MeV. The Δ-resonance peak is seen at photon energies ~300 MeV. Together with the mass energy of a nucleon, the resulting Δ has an enrgy around 1232 MeV.

These gamma-ray induced resonances result in the production of fast neutrons.

1.4 Project motivation

The purpose of this project was to investigate fast photoneutron production from a series of materials commonly used for backing thermal-neutron beam guides, such as aluminium, copper and steel. At a neutron spallation source, these materials get exposed to high-energy gamma-rays coming from the spallation target and moderator. These high-energy gamma-rays interact with the backing materials, spraying unwanted fast neutrons into the experimental endstations. In this measurement, the experimental geometry was well-defined. Thus the probability for fast-neutron photoproduction could be precisely measured. By eventually comparing these data to a detailed simulation suite tuned exactly to this experimental setup, validation benchmarks will be obtained. A well-defined and well-controlled validation benchmark where simulations can be rigorously tested against data is crucial to establishing the believability of the software efforts.

Chapter 2

Materials and Methods

2.1 Photon Tagging

In 1986, the first electron accelerator and pulse-stretcher at MAX-lab were commissioned. In this experiment, the apparatus was used to send a continuous wave (CW) beam of electrons to the Photon-Tagging Facility shown in Fig. 2.1.

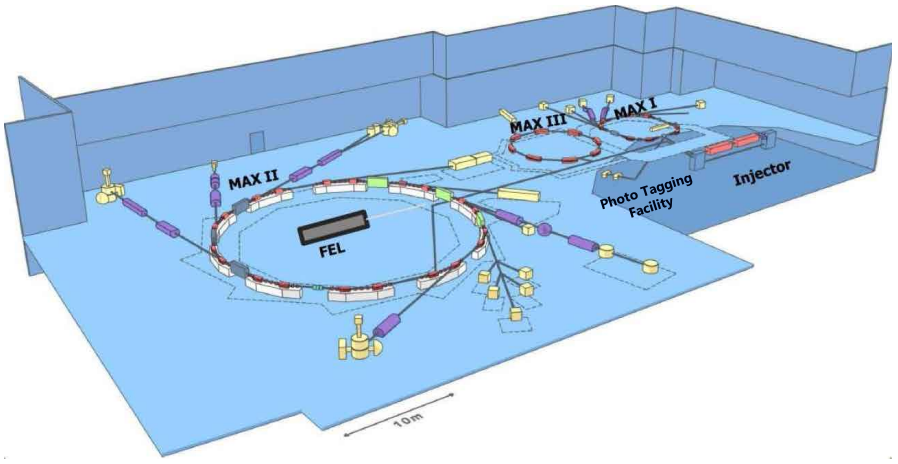

FIGURE 2.1: An overview of the MAX-lab facility. Free electrons are created in the injector and accelerated and injected into one of three storage rings. MAX I was built first and has a circumference of 32.4 m. MAX II is the largest storage ring with a circumference of 90 m. MAX III was built in 2007. The photon-tagging facility is located in the basement beneath MAX I.

At the Photon-Tagging Facility, the first step was to convert some of the electrons in the CW electron beam to photons. The CW electron beam was directed onto a 300 μm aluminium target, called a "radiator". The radiator was used to radiate a small partion of the electrons in the CW electron beam. When electrons radiated with the aliminium a

portion of the kinetic energy of the radiating electrons were lost as photons, in a process called “bremsstrahlung”.

Electrons that passed through the radiator without interacting were dumped. A magnetic field bent the post-bremsstrahlung electrons, as shown in Fig. 2.2. The magnetic field resulted in a Lorentz force being applied to the electrons according to

$$\vec{F}_{\mathrm{L}} = e \cdot (\vec{E} + \vec{v} \times \vec{B}), \tag{2.1}$$

where $\vec{F}_L$ is the Lorentz force, e is the electron charge, $\vec{E}$ is the electric field (zero), $\vec{v}$ is the velocity of the electron and $\vec{B}$ is the magnetic field. The more energy an electron lost to the radiation of a photon, the less momentum it has remaining and the more it is bent by the magnetic field. The trajectory is thus a function of the momentum of the recoiling electron. The recoiling electrons were detected in an array of 62 plastic scintillators. The difference between the energy of the incoming electron beam, $\mathrm{E_{beam}}$, and the energy of the recoiling electron, $\mathrm{E_{recoil}}$, equals the energy of the radiated photon, $\mathrm{E_{\gamma}}$, given by

$$E_{\gamma} = E_{\mathrm{beam}} - E_{\mathrm{recoil}}. \tag{2.2}$$

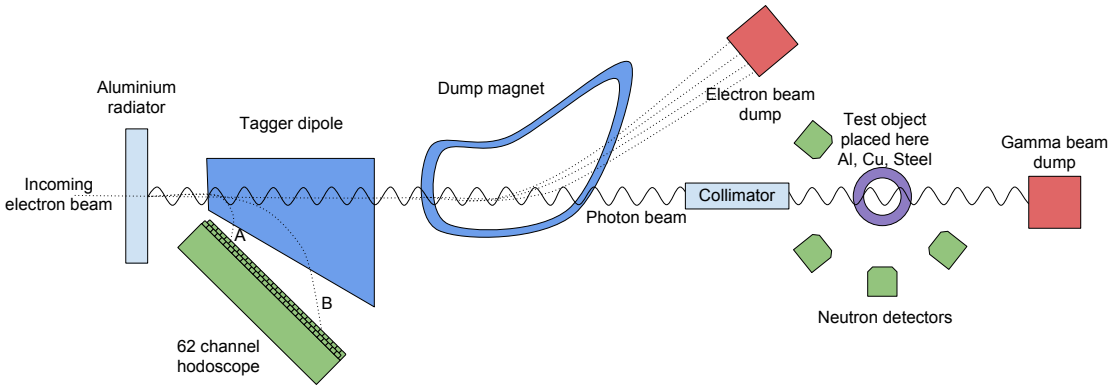

FIGURE 2.2: Electrons produce bremsstrahlung photons in the aluminium radiator. The radiated electrons were deflected by a magnetic field and directed into a 62 channel hodoscope. Electron A corresponded to a much higher energy photon than electron B. Unradiated electrons were dumped. The photons passed through the collimator to the test object. Neutron detectors registered the resulting fast photoneutrons at different angles around the test object.

The recoil-electron detector was a 62 channel plastic-scintillator hodoscope which registered electrons corresponding to the photon energies listed in Table 2.1. The hodoscope is shown in Fig. 2.3.

TABLE 2.1: The 62 hodoscope channels and corresponding photon energies. The 62 channels have been divided into 8 bins which will be reported on for the remainder of this work.

Channel	Bin	Photon energy (MeV)	Channel	Bin	Photon energy (MeV)
1	8	66.31	33	4	37.04
2		65.48	34		36.01
3		64.65	35		34.96
4		63.82	36		33.91
5		62.98	37		32.85
6		62.14	38		31.78
7		61.29	39		30.69
8		60.43	40		29.60
9	7	59.57	41	3	28.50
10		58.71	42		27.38
11		57.84	43		26.26
12		56.96	44		25.12
13		56.08	45		23.97
14		55.19	46		22.81
15		54.30	47		21.64
16		53.40	48		20.46
17	6	52.49	49	2	19.26
18		51.58	50		18.05
19		50.66	51		16.83
20		49.74	52		15.59
21		48.80	53		14.34
22		47.87	54		13.07
23		46.92	55		11.79
24		45.97	56		10.50
25	5	45.01	57	1	9.19
26		44.04	58		7.86
27		43.06	59		6.52
28		42.08	60		5.17
29		41.09	61		3.79
30		40.09	62		2.40
31		39.08			
32		38.07			

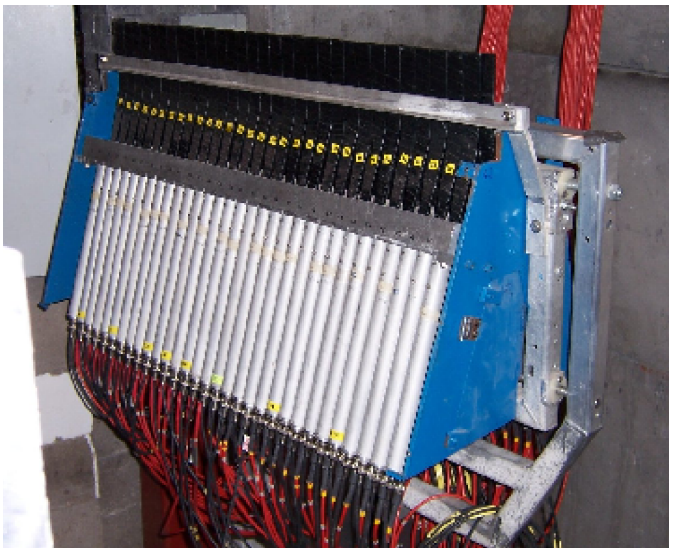

FIGURE 2.3: The 62 channel plastic-scintillator hodoscope used at the MAX-lab photon-tagging facility. To supress background, the 62 scintillators are aligned in two overlapping rows half covering each other and a coincidence between the overlapping detectors is required. Figure courtesy K. Fissum.

2.2 Neutron detectors

2.2.1 Organic liquid scintillators

A scintillator is a material that converts ionizing radiation to visible light. The electrons of the atoms and molecules of the scintillator are excited or even ionized by the incoming radiation. Ionization leads to further ionization and excitation. Most importantly, de-excitation leads to a flash of light. As the excited state of the scintillators can be meta-stable, de-excitation can take from a few ns to hours. Different scintillators respond differently to different types of ionizing radiation.

Organic liquid scintillators are a popular choice for detecting fast neutrons. NE-213 is an organic liquid scintillator that consists of Xylene, C_8H_{10}, which has a large number of hydrogen atoms. Hydrogen has a large (n, p) cross section. Neutrons scattering from the hydrogen nuclei result in the recoiling hydrogen nuclei exciting the scintillator. This leads to a relatively long lasting flash of light. NE-213 is unfortunately also quite sensitive to gamma-rays, which Compton scatter from the scintillator electrons (see Section 3.1.1) and also create scintillation light. The Compton-scattered electrons result in short pulses of scintillation light. The differences in the scintillation time constants for gamma-rays and neutrons can be used to distinguish the two particle spicies.[1]

[1] EJ-305 is another organic liquid that scintillates when irradiated with fast neutrons. It is based on highly purified pseudocumene and has a very high light output. Pseudocumen is 1,2,4-trimethylbenzene ($C_6H_3(CH_3)_3$), a flammable, colorless aromatic hydrocarbon.

2.2.2 Photomultipliers

When scintillators were first used in 1903, the light emitted was registered by eye. In 1944, the Photo-Multiplier Tube (PMT) was invented. Today, PMTs replace our eyes. A scintillator coupled to a PMT is shown in Fig. 2.4. The photons created in the scintillator by the incident radiation pass into the PMT through an optical window which is followed by a photocathode. At the photocathode, the scintillation photons free electrons via the photoelectric effect[2]. These freed photoelectrons are focused by an electrode and electrostatically accelerated towards a series of dynodes. At each dynode the incident electrons are multiplied, such that a single photoelectron from the photocathode can result in millions of electrons at the final dynode, which is called the "anode". The electrical signal produced by the PMT is very fast (ns risetime) and is proportional to the energy of the incoming radiation.

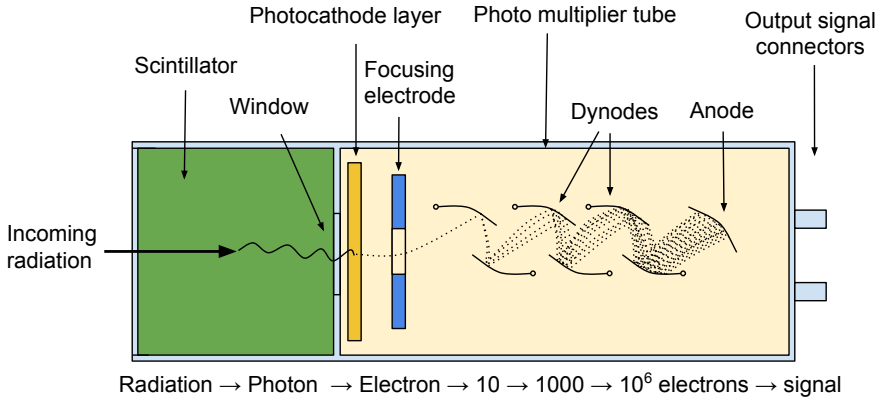

FIGURE 2.4: A scintillator detector coupled to a PMT. Incoming radiation results in a scintillation photon. The photon passes through the optical window, interacting with the photocathode layer by the photoelectric effect. The photoelectron is focused and accelerated across the dynodes by an electric field and multiplied at each step. The resulting signal is presented at the anode and is proportional to the energy of the incoming radiation.

2.2.3 Configuration

The neutron detectors employed in this experiment included:

- **Nordball** detectors, placed at nominal laboratory angles of 45°, 90° and 135° from the beam. These detectors were filled with NE-213 liquid scintillator. The scintillator faces were shaped either as pentagons or hexagons.

[2]Photons with sufficient energy can be photoelectrically absorbed by atomic electrons. This results in an ejected photoelectron.

- **NE-213 Sjögren** detector was a cubic 122×122×179 mm^3 cell filled with NE-213 liquid scintillator.
- **NE-213 cup** detector was a cylindrical cell filled with NE-213 liquid scintillator. The circular face had a diameter of 94 mm and was 62 mm deep.
- **EJ-305 cup** detector was a cylindrical cell filled with EJ-305 liquid scintillator. The circular face had a diameter of 94 mm and was 62 mm deep.

The Sjögren and cup detectors were placed at a laboratory angle of about 135°. Photos of the detectors are shown in Fig. 2.5. The experimental configuration is shown in Fig. 2.6.

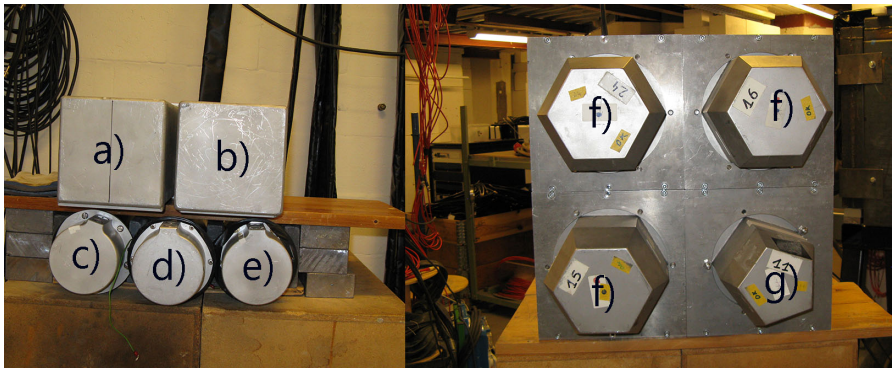

FIGURE 2.5: The detectors used: **a)** Sjögren **b)** Not used **c)** Not used **d)** NE-213 cup **e)** EJ-305 cup **f)** Hexagonal Nordball **g)** Pentagonal Nordball

2.3 Electronics

2.3.1 Signal-processing basics

Charge-to-digital convertors (QDCs) are devices that can integrate currents. The integral of the current pulse from a PMT is equal to the charge carried by the signal and is proportional to the energy deposited in the detector by the neutron. A PMT current pulse registered in a QDC is shown in Fig. 2.7. The integration starts at the time T_1 when the gate signal opens and stops at T_2 when the gate signal closes. The charge Q is then

$$Q = \int_{T_1}^{T_2} dt \cdot i(t) \tag{2.3}$$

where t is time and i is current.

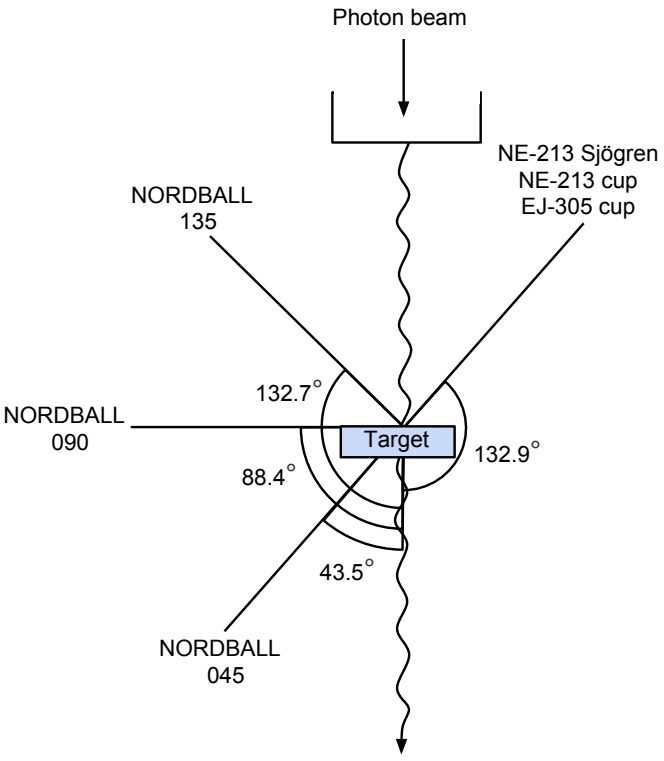

FIGURE 2.6: Top view of the experiment. The photon beam struck the target at normal incidence. Around the target, three Nordball arrays were placed at angles 43.5°, 88.4° and 132.7°. The NE-213 Sjögren, NE-213 cup and EJ-305 cup detectors were placed 132.9° from the incident photon beam.

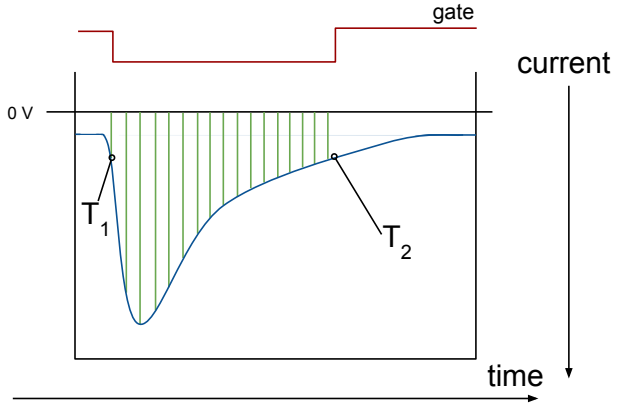

FIGURE 2.7: A current signal sent from a PMT to be integrated in a QDC. When the gate opens at time T_1, the QDC starts integrating the signal. The green area, the charge output of the PMT, is proportional to the energy that was deposited into the PMT.

2.3.2 Threshold

The minimum signal required to trigger a detector is set with a discriminator. The energy limit enforced by the discriminator is called the "threshold". Photons or neutrons depositing energy below the threshold will not create a trigger. This results in the cut-off illustrated in Fig. 2.10. Setting the threshold too low means that the actual events of interest may be lost in a flood of uninteresting low-energy background. Setting the threshold too high also means that the actual events of interest may be lost. In Fig. 2.8, two different thresholds are shown. The higher discriminator setting B would not register the low amplitude red pulse whereas discriminator setting A would register both pulses.

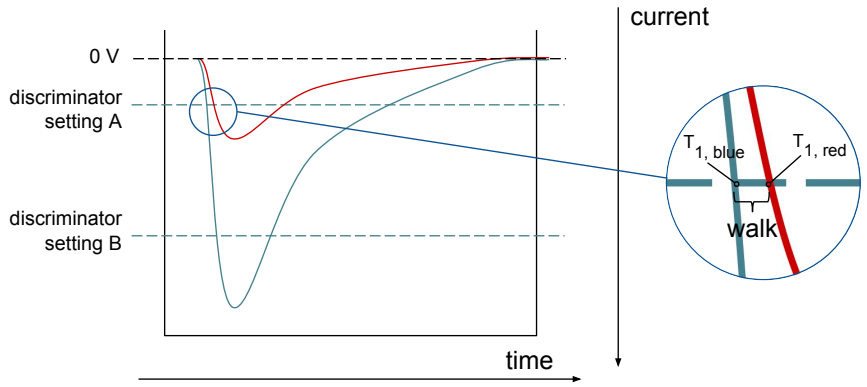

FIGURE 2.8: Two current pulses registered in a QDC. The red pulse with lower amplitude comes from a neutron or gamma ray that deposited less energy in the detector than occurred with the larger, blue pulse. Discriminator setting B would only trigger on the blue pulse. Discriminator setting A would trigger on both pulses, with a small difference in timing, known as discriminator "walk" between $T_{1,\mathrm{blue}}$ and $T_{1,\mathrm{red}}$.

2.3.3 Pedestal

If one detector fires, a common gate is presented to all of the detector QDCs, even those which did not register an event. The QDCs corresponding to the detectors which did not trigger will integrate their offsets and report a pedestal count, see Fig. 2.9. These pedestal peaks will therefore contain many more counts than the event peaks, as in Fig. 2.10.

2.3.4 Walk and constant-fraction discriminators

As seen in Fig. 2.8, there is a difference in T_1 between the low amplitude red signal and the higher amplitude blue signal. This variation in signal timing leads to discriminator "walk". One cannot correct for walk in the data analysis. Optimally, the timing of a

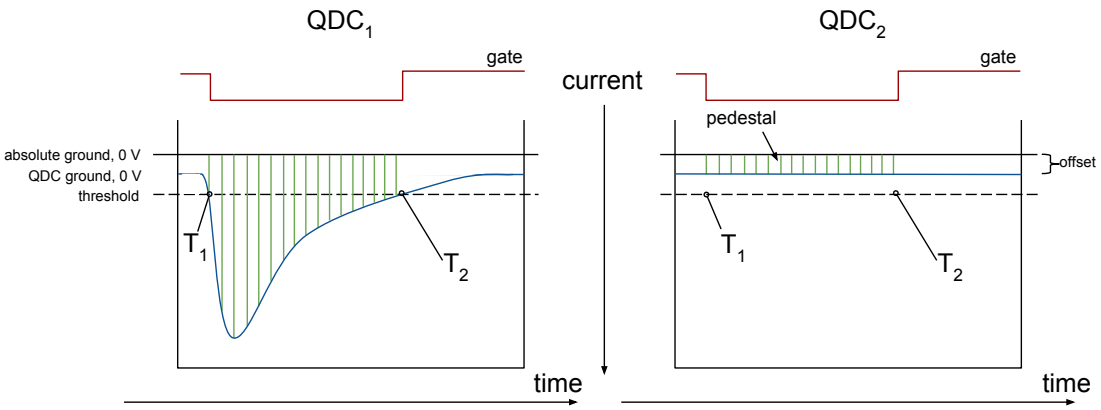

FIGURE 2.9: QDC_1 registers an event with energy above the threshold and integrates the corresponding signal from T_1 to T_2. As the gate is common, QDC_2 also integrates from T_1 to T_2, effectively determining the charge in the offset. This so-called pedestal event establishes the zero level in QDC_2.

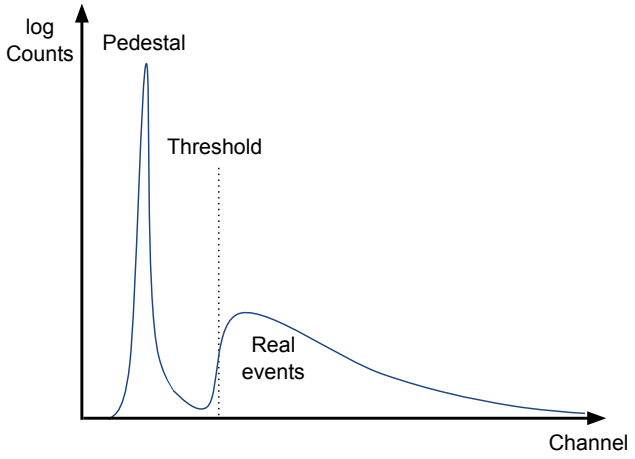

FIGURE 2.10: An example spectrum illustrating pedestal, threshold and real events. The high pedestal or "QDC-zero" peak results from events registered in other detectors. Below threshold, no events apart from the pedestal are registered. The real events registered in this detector are in the wider peak, to the right of the threshold.

signal should be independent of the amplitude. One solution to eliminate walk is to use Constant Fraction Discriminators (CFDs). Here, the input analog signal is split, inverted and delayed and then resummed, see Fig. 2.11. By triggering on the zero-crossing point rather than the signal height, a walk-free timing spectrum may be achieved.

2.3.5 Schematic

A schematic illustration of the experiment setup is shown in Fig. 2.12. If an event was detected in one of the 13 detectors used, a signal pulse was sent from that detector. This signal pulse was split. One signal was delayed and passed directly to a QDC for

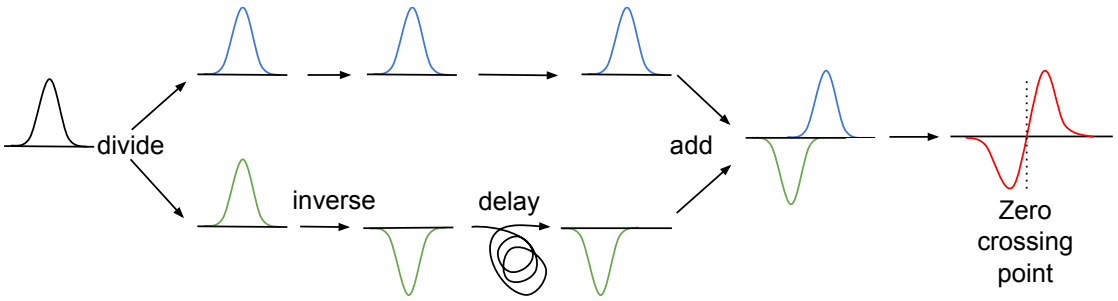

FIGURE 2.11: The workings of a CFD. The initial black signal is split. The green portion is inverted, delayed and then summed with the blue signal to become the rightmost red signal. The zero-crossing point may be used for walk-free timing.

integration. The other signal was passed to a CFD to build the trigger. From the CFD, the signal was folded in an OR with those provided by other detectors to create the "X-trigger". The X-trigger set the LATCH. The LATCH was used to reject any further X-trigger signals from the OR-logic until the present data-collection cycle was completed. The LATCHED X-trigger was used to gate the QDCs and start the 62-channel hodoscope time-to-digital converters (TDCs). A TDC can measure time by counting the number of oscillations of an oscillating crystal of a known frequency. Using long cables the signals from the hodoscope was delayed ~250 ns and used to stop the TDCs. An additional delay of 125 μs after the LATCH allowed for all of the analog-to-digital conversions to be performed at which point the data-acquisition system was polled by the data-acquisition computer. Once the data had been read and cleared, the LATCH was reset, opening up the data-acquisition system for the next event to be registered.

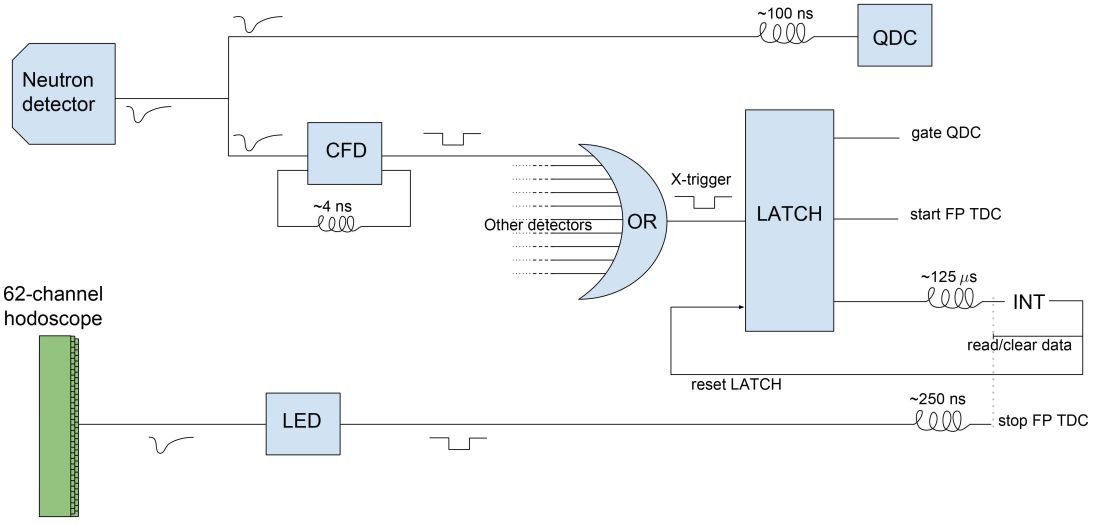

FIGURE 2.12: A simplified schematic of the experiment setup. When a detector registered an event, the resulting X-trigger set the LATCH and initiated signal processing. Once the data were transferred to the computer, the LATCH was reset.

2.4 Calibration sources

Am/Be and ThC sources were used for calibrations of the detectors.

2.4.1 Am/Be

Americium is a radioactive metal with atomic number 95. It is not naturally occurring but is synthesised from plutonium. The isotope ^{241}Am has a half-life of 432.2 years. ^{241}Am decays via α emission. Beryllium is a naturally occurring metal with atomic number 4. ^{9}Be can interact with α particles resulting in ^{12}C and a free neutron. In the 1950s, americium-oxide powder and ^{9}Be powder were first combined, creating a free-neutron source. With the long half-life of ^{241}Am, such Am/Be sources give a steady flux of neutrons for many years.

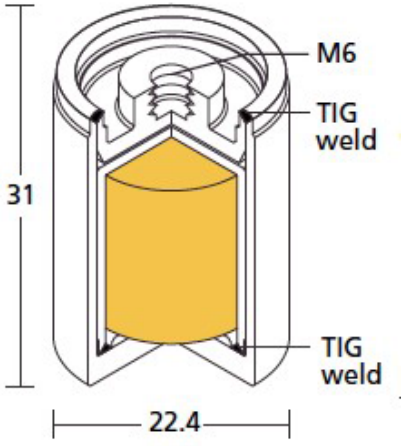

FIGURE 2.13: An illustration of the Am/Be source used. The two-layered stainless steel capsule holding the Am/Be (yellow) is welded shut. Dimensions are in mm. Figure from https://www.hightechsource.co.uk/.

The resulting ^{12}C is created in its ground, first excited or second excited state. Calculations by Vijaya and Kumar[4] suggest that the relative populations of these states are ~35%/~55%/~15% respectively. When ^{12}C is created in its first excited state, it promptly de-excites to the ground state, isotropically emitting a 4.44 MeV gamma-ray.

2.4.2 Thorium-C

Thorium is a metal with atomic number 90 and is one of the three naturally occurring radioactive elements on earth. Almost all thorium present in nature is found as

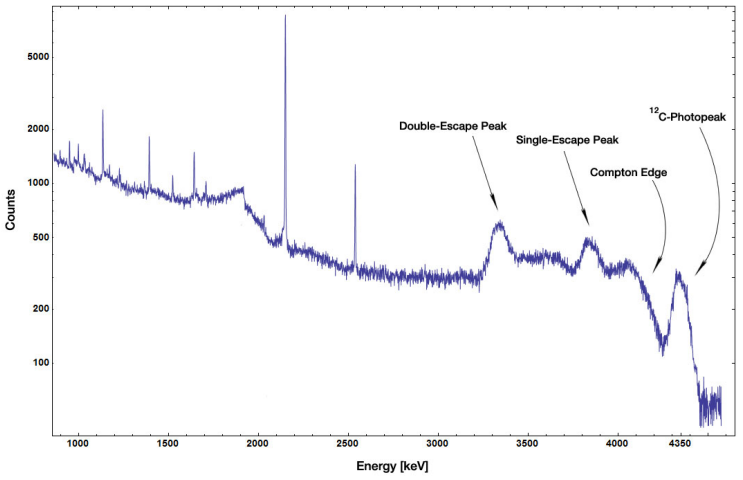

FIGURE 2.14: The gamma spectrum from an Am/Be source obtained using a high-resolution HPGe detector. Note the strong 4.44 MeV peak from relaxation of first state excited ^{12}C. The Compton edge of the 4.44 MeV gamma is seen at 4.20 MeV. The peaks at 3.93 MeV and 3.42 MeV are the first and second escape peaks corresponding to the 4.44 MeV gamma-ray. Figure from [5].

^{232}Th, which is relatively stable with a half-life of 14 billion years. From naturally occurring ^{232}Th, the thorium decay series goes through multiple elements. For historical reasons, elements of the decay series have received thorium "subtitles". For example, one intermediate element of thorium decay, ^{216}Po, is also called thorium-A (ThA). The last few transitions before the end of the thorium chain (^{208}Pb) are shown in Fig. 2.15. The element ^{212}Pb (ThB) β-decays to ^{212}Bi, also called ThC. ThC has ~65% chance of β-decaying and ~35% chance of emitting a 6.20 MeV α particle. 100% of the atoms starting the α-chain from ThC will continue to β-decay to ThD (^{208}Pb*), and then emit a 0.58 MeV gamma-ray and a 2.62 MeV gamma-ray in a cascade to become stable ^{208}Pb. The 2.62 MeV gamma-ray from this de-excitation is very useful for calibrations of gamma-ray detectors.

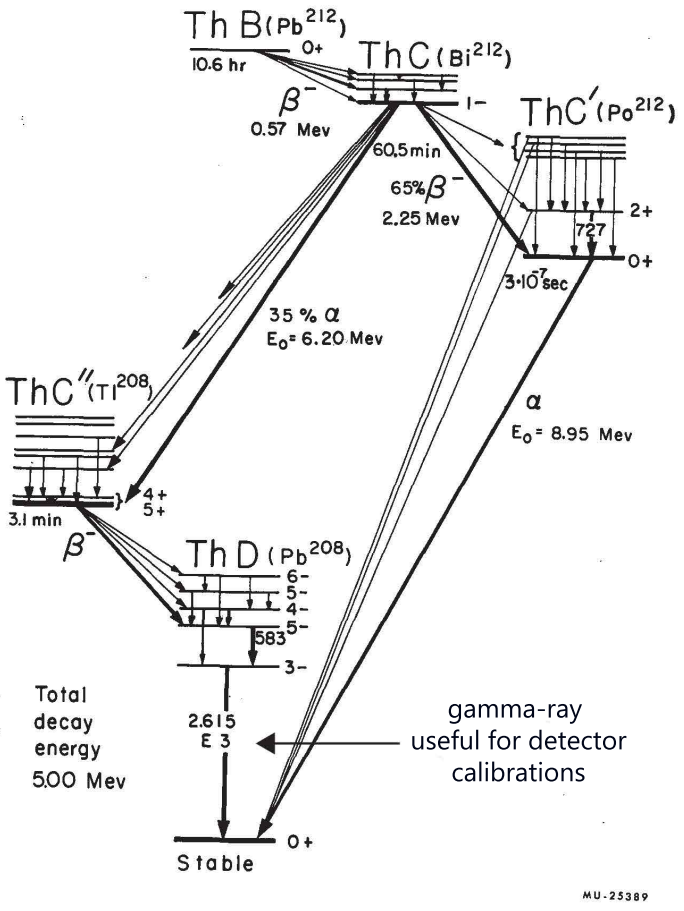

FIGURE 2.15: The decay schemes from ThC to stable ^{208}Pb. 35% of the decays from ThC are by emitting a 6.20 MeV α particle. This path leads to the excited ThD (^{208}Pb*) which relaxes to stable ^{208}Pb via the emission of a 2.62 MeV gamma-ray. Figure taken from [6].

Chapter 3

Data Analysis, Results and Discussion

The analysis followed the flow chart shown in Fig. 3.1. The first step was to define the exact locations of the Compton edges in the gamma-ray calibration spectra. These allowed for the detector energy calibrations to be performed. With the energy calibrations in hand, it was possible to determine the hardware thresholds of the detectors in units of MeV_{ee}[1]. Moreover, the thresholds could then be varied as input in simulations that evaluated the neutron-detection efficiency.

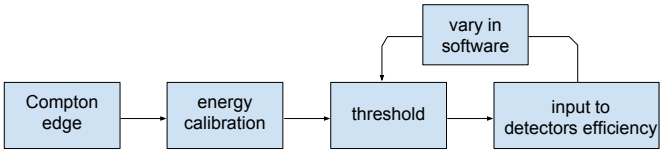

FIGURE 3.1: An analysis flow chart. For each detector, the Compton edge in the gamma-ray calibration spectra was found, which allowed for energy calibrations to be made. After that, the hardware thresholds were determined and used in simulations of the neutron-detection efficiency of the detectors. Finally, the neutron-detector thresholds were varied in the software in order to study their optimal values.

[1]Note that MeV_{ee} (electron equivalent) is a unit measuring how much energy the ionization electrons deposit in a detector rather than how much energy the incoming radiation had, which is typically quoted in MeV.

TABLE 3.1: Compton-edge energies of Am/Be and ThC gamma-rays.

	Gamma-ray energy (MeV)	Compton-edge energy (MeV)
Am/Be	4.44	4.20
ThC	2.61	2.24

3.1 Calibrations

3.1.1 Compton edges and thresholds

When a photon strikes a barely bound electron in an atom, it can transfer some of its energy into freeing the electron. This is called Compton scattering. The energy transferred to the electron is proportional to the angle of the scattered photon. Most energy is transferred if the incoming photon is scattered 180° from its original course. A scatter through a smaller angle transfers less energy to the electron. The maximum energy an electron can absorb in a single Compton scatter is given by

$$E_{\max} = \frac{2E_\gamma^2}{m_0c^2 + eE_\gamma}, \tag{3.1}$$

where $E_{\max}$ is the Compton-edge energy, E_γ is the energy of the incident photon, and m_0c^2 is the energy of the rest mass of the electron, see Fig. 3.2.

The Compton edges corresponding to the 4.44 MeV Am/Be gamma-ray and the 2.61 MeV ThC gamma-ray are presented in Table 3.1.

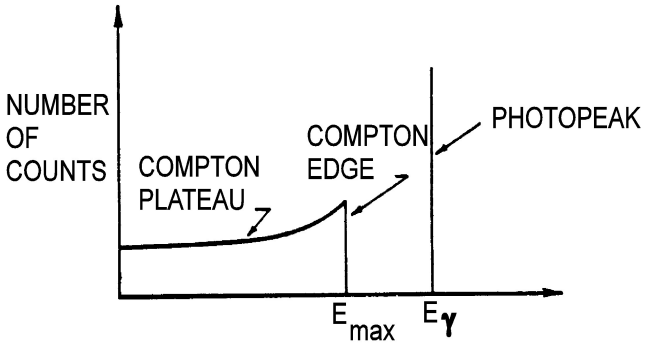

FIGURE 3.2: An idealized gamma-ray spectrum showing the Compton-edge effect. E_γ marks the energy of the incident gamma-ray. $E_{\max}$ is the maximum energy transferable by Compton scattering and is the position of the Compton edge. The Compton plateau corresponds to Compton scatters which deposit less than $E_{\max}$. Figure from [7].

As discussed in detail in Nilsson [8], because detectors have finite energy resolution, the Compton edge will generally be smeared out and not seen as the sharp cutoff shown

in Fig. 3.2. There are many different methods of determining the exact location of the Compton edge in a realistic, resolution-limited set of data. In this work, two methods were employed and compared. The first method was developed by K. F. Flynn [9] and the other by H. H. Knox [10]. Flynn suggests that 104% of the maximum transferred energy in Compton scattering is located at 50% of the height of the resolution-smeared Compton-edge distribution while Knox suggests that the maximum transferred energy from Compton scattering is at 89% of the same, see Fig. 3.3.

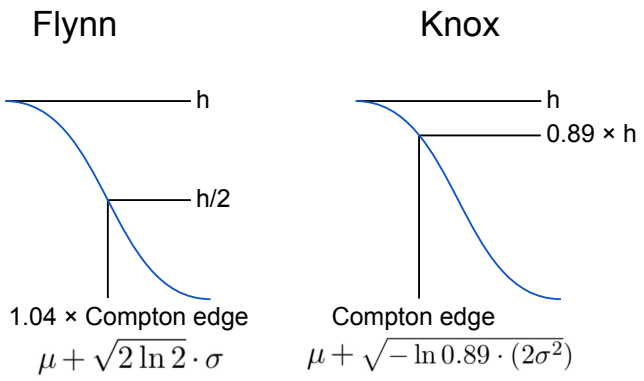

FIGURE 3.3: Illustrations of the methods of locating the Compton-edge location from a Gaussian distribution representing the resolution-smeared Compton edge suggested by K. F. Flynn and H. H. Knox. Flynn positions 104% of the energy of the Compton edge at half of the total height of the Gaussian ($\mu + \sqrt{2 \ln 2} \cdot \sigma$). Knox suggests that the full energy of the Compton edge is located at 0.89 times the total height of the Gaussian ($\mu + \sqrt{-\ln 0.89 \cdot (2\sigma^2)}$).

By applying the methods discussed above for determining the locations of the Compton edges in the source gamma-ray spectra, the detectors were calibrated for energy. For the calibrations, an Am/Be source was placed in front of each of the detectors for a series of one-hour measurements on four different days distributed evenly throughout the month-long experiment. The procedure was repeated using ThC. The resulting spectra were fitted with Gaussian functions. Using the mean μ and variance σ of the fits, it was possible to locate the channel numbers corresponding to 50% and 89% of the height of the distributions. The threshold values can be extracted from the spectra in essentially the same way, fitting the threshold edges with Gaussian functions and calculating their values at half of the height. Figure 3.4 shows an Am/Be source spectrum overlayed with Gaussian fits and dashed lines marking the threshold and 50% and 89% height of the Compton-edge fit.

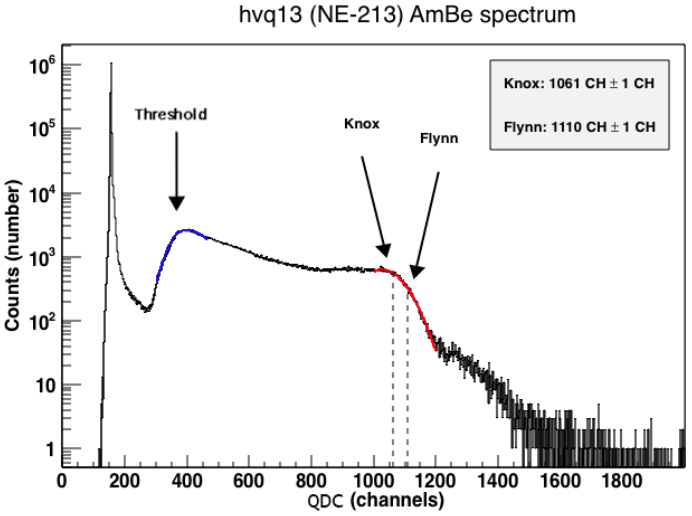

FIGURE 3.4: A spectrum gathered with the NE-213 cup using the Am/Be source. The leftmost peak is the pedestal. The threshold edge is fitted with a Gaussian function in blue and the Compton edge is fitted with a Gaussian function in red. Both the 89% mark of the Knox method and the 50% mark from the Flynn method of identifying the location of the Compton edge are marked with dotted lines.

3.1.2 Fits

Figures 3.4 and 3.5 show sample results for Am/Be and ThC obtained with the NE-213 cup. In each Fig., the pedestals, thresholds, fitted functions and Compton edges are easily identified. These figures are representative of the entire data set. Figure 3.4 shows the data from an hour of Am/Be exposure. The structure around channel 1100 is the Compton edge corresponding to the 4.44 MeV gamma-ray. The structure at channel 150 is the pedestal and the structure around channel 300 is the threshold. Figure 3.5 shows the data from an hour of ThC exposure, where the 2.61 MeV ThC gamma-rays induce the Compton edge around channel 700. The pedestal at channel 150 and threshold at channel 300 are at the same positions as with the Am/Be source in Fig. 3.4.

3.1.3 Energy Calibration

The next step in the data analysis was to employ the locations of the Compton edges determined from the measured spectra to calibrate them for energy. The channel numbers and energy deposited in the detector, expressed in the unit MeV_{ee}, are related through

$$E[\mathrm{MeV}_{ee}] = E[\mathrm{channel}] \cdot \mathrm{gain}[\mathrm{MeV}_{ee}/\mathrm{channel}] + \mathrm{constant}[\mathrm{MeV}_{ee}], \tag{3.2}$$

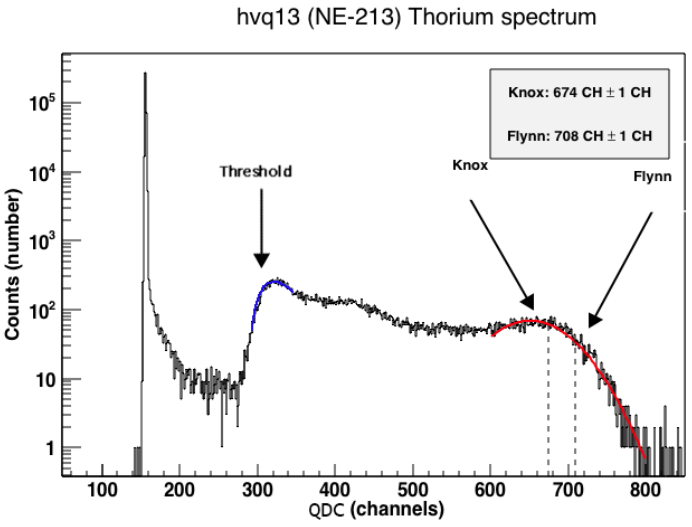

FIGURE 3.5: A spectrum gathered with the NE-213 cup using the Thorium source. The leftmost peak is the pedestal. The threshold edge is fitted with a Gaussian function in blue and the Compton edge is fitted with a Gaussian function in red. Both the 89% mark of the Knox method and the 50% mark from the Flynn method of identifying the location of the Compton edge are marked with dotted lines.

where E[channel] is the channel number of a point in the spectrum, E[MeV$_{ee}$] is the corresponding electron equivalent of the energy at that point and gain[MeV$_{ee}$/channel] is a unique number of MeV$_{ee}$ per channel for each detector. Plotting E[MeV$_{ee}$] against E[channel] will make a plot in which the slope is the gain[MeV$_{ee}$/channel]. The channel numbers of the Compton edges (as shown in Fig. 3.4 and 3.5) and their corresponding energies from Table 3.1 as well as the pedestal position for 0 MeV$_{ee}$ form this linear relation as predicted by Eq. 3.2 and as shown in Fig. 3.6. The Flynn and Knox methods for determining the energy calibrations agree very well, differing at most 1.5%. Based on the GEANT4[2] simulations and a detailed evaluation by Scherzinger et al [12], the Knox method was employed for the remainder of this thesis. The resulting calibration functions for each of the detectors obtained using the Knox method are presented in Appendix C.

3.1.4 Energy-Calibrated Thresholds

The next step in the analysis was to determine the thresholds of the detectors in MeV$_{ee}$. In Figures 3.7 and 3.8, calibrated data obtained with the NE-213 cup using the Am/Be and ThC sources are shown. From this type of plot, the threshold of the detector was determined. The threshold position was located by fitting the threshold shoulders of the Am/Be and ThC data with Gaussian functions and then calculating the average value

[2]GEANT4 [11] is a toolkit for simulating the passage of particles through matter.

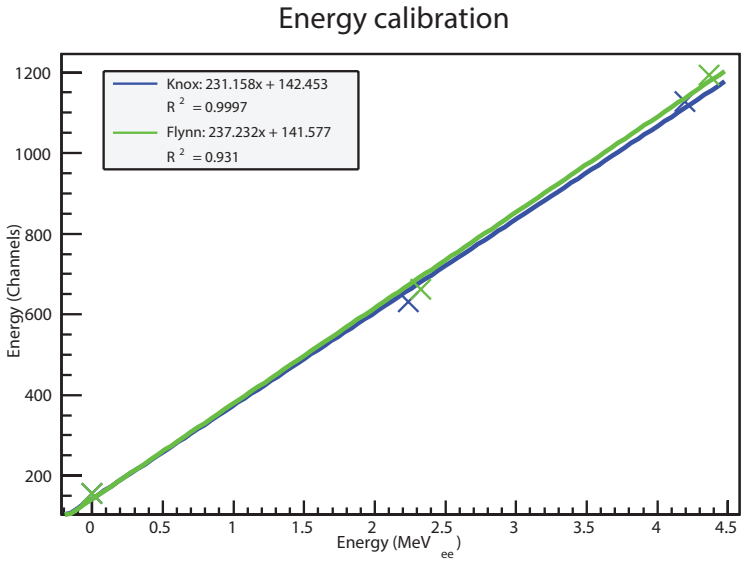

FIGURE 3.6: Conversion between channels and energy for the NE-213 cup. The positions of the Compton edges have been localized as defined according to Flynn, in green, and Knox, in blue. The green Flynn fit shows a 0.003% larger slope. The residual variance of the fits, R^2, is higher for the Knox calibration. A higher R^2 means better compliance between the fit and the data points.

of where both fits had their half-heights. For example for the NE-213 cup, the average threshold found from the two sources was 0.78 MeV_{ee}.

The thresholds determined from the four days of calibrations throughout the month are presented in Fig. 3.9 and Table 3.2. The consistency of all the 5″ Nordball detectors was very good throughout the month. This was because they were all connected to a brand new high voltage power supply CAEN [13] which was very stable. The Sjögren detector wandered the most with a variance of 560 keV_{ee}, the NE-213 cup varied 360 keV_{ee} and the EJ-305 cup showed a variation of 190 keV_{ee} in threshold. This was because they were connected to a 30-year old LeCroy high voltage power supply [14] that is starting to show its age. Gain drifts may be corrected for in software.

3.2 Simulations of neutron-detection efficiency

3.2.1 Typical input

The efficiency of a detector is the property that determines how many of the incident particles are detected. By dividing the number of detected particles, N_{detected}, by the detection efficiency, ε, the true number of particles, N_{true}, may be found according to

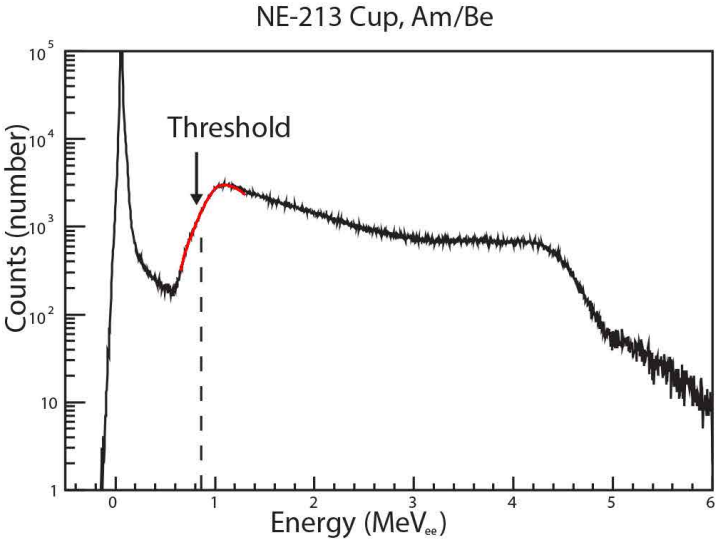

FIGURE 3.7: Energy-calibrated source data from Am/Be collected using the NE-213 cup. The Gaussian fit is shown in red. The threshold position is marked with a dotted line at half the height of the fitted Gaussian, 0.86 MeV$_{ee}$.

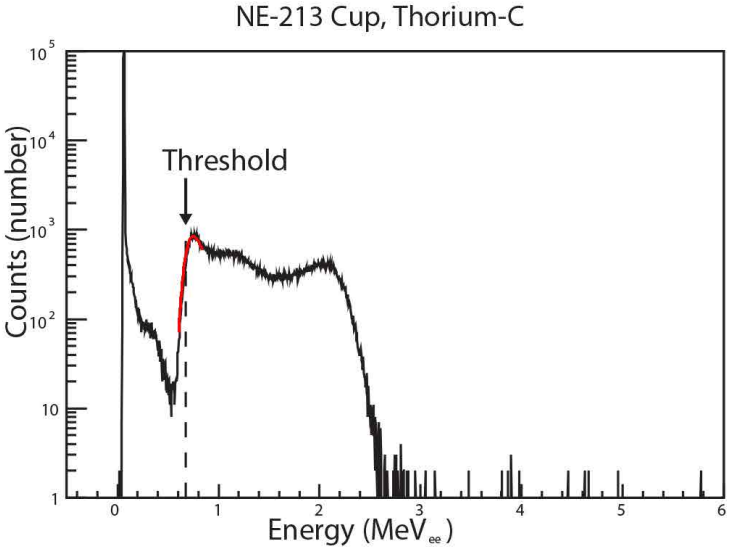

FIGURE 3.8: Energy-calibrated source data from ThC collected using the NE-213 cup. The Gaussian fit is shown in red. The threshold position is marked with a dotted line at half the height of the fitted Gaussian, 0.67 MeV$_{ee}$.

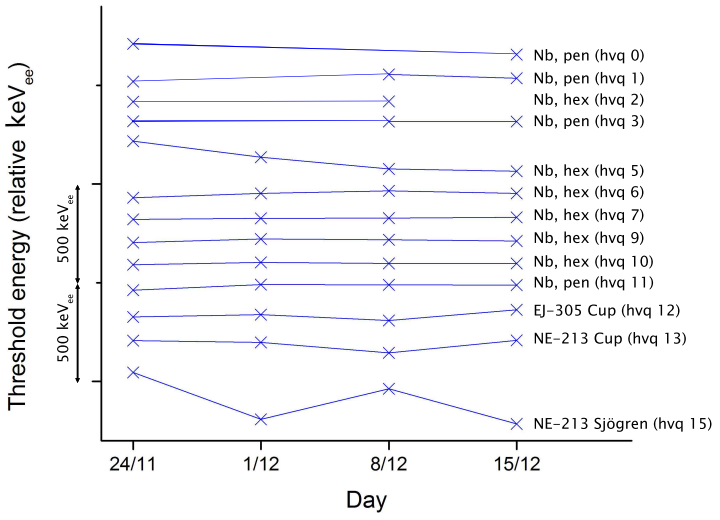

FIGURE 3.9: The stability of the detector thresholds throughout the month-long experiment. The threshold values from differnet detectors have been given offsets along the threshold axis. Changes in thresholds throghout the month are seen but no absolute threshold values can be read from this graph. All the Nordball detectors show stable behaviour.

TABLE 3.2: The hardware thresholds in MeV$_{ee}$ determined using the source calibrations.

hvq	Detector	Threshold (MeV$_{ee}$)			
		24-Nov	01-Dec	08-Dec	15-Dec
hvq 0	Nordball, pentagonal	0.96	-	-	0.91
hvq 1	Nordball, pentagonal	1.10	-	1.14	1.12
hvq 2	Nordball, hexagonal	1.12	-	1.12	-
hvq 3	Nordball, pentagonal	1.23	-	1.23	1.23
hvq 5	Nordball, hexagonal	1.01	0.93	0.87	0.86
hvq 6	Nordball, hexagonal	1.22	1.24	1.25	1.24
hvq 7	Nordball, hexagonal	1.21	1.22	1.22	1.22
hvq 9	Nordball, hexagonal	1.11	1.13	1.13	1.12
hvq 10	Nordball, hexagonal	1.22	1.24	1.23	1.23
hvq 11	Nordball, pentagonal	1.12	1.15	1.15	1.15
hvq 12	EJ-305 cup	0.36	0.38	0.35	0.40
hvq 13	NE-213 cup	0.77	0.76	0.71	0.77
hvq 15	NE-213 Sjögren	1.05	0.81	0.96	0.78

$$N_{\text{detected}} = N_{\text{true}} \cdot \varepsilon. \tag{3.3}$$

Precise knowledge of the detection efficiency often requires detailed computer simulations. In this work, a fast neutron Monte Carlo simulation named the Stanton code [15] was used. The Stanton code was first written in 1971 and has been improved many times since. The version used here is the Kent State University version [16]. This code can simulate different detector geometries, threshold energies and densities of hydrocarbon scintillators, such as NE-213. It is based on experimentally measured cross sections for many neutron-reaction channels, the most predominant one being *np* elastic scattering.

The simulations were run for neutron kinetic energies from 0 MeV to 70 MeV to cover the entire range of neutron energies shown in Table 3.3. The geometries used were either cubic or cylindrical as shown in Fig. 3.10. The pentagonal and hexagonal Nordball detectors were approximated as cylinders with radii determined from the average distance from the centers of the detectors to their edges.

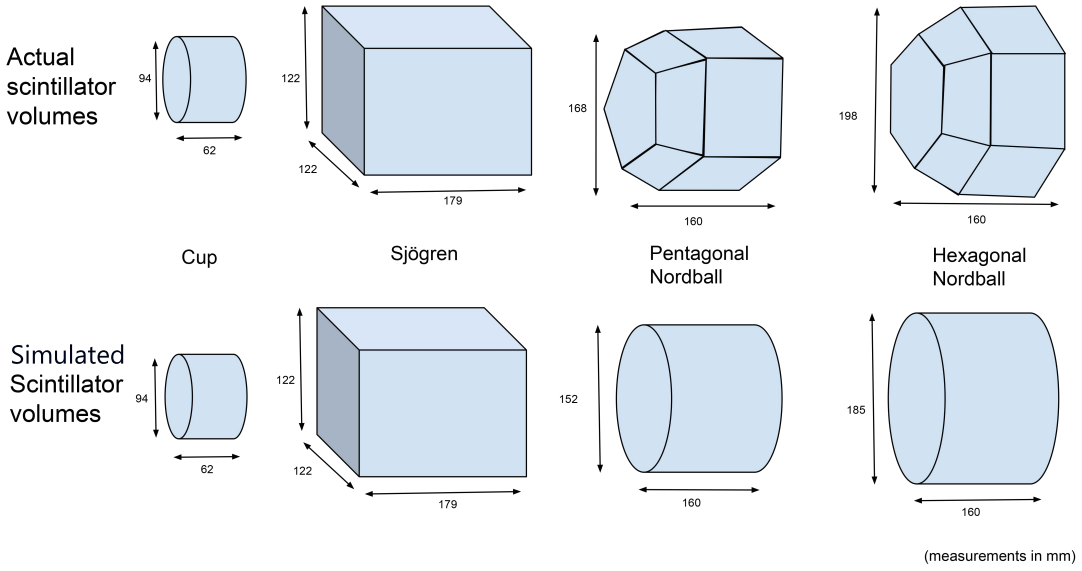

FIGURE 3.10: Models of the detectors including both actual and simulated dimensions.

Electrons, protons and neutrons deposit different amounts of energy in liquid scintillators for the same distance travelled. Relative light-response transformation functions describe the relationships between them. A gamma-ray will interact almost only with atomic electrons in a scintillator. Reacting directly with electrons create a maximised light output. Neutrons react mostly with hydrogen nuclei, which then in turn can interact with electrons and create light. This results in a lower light output per unit incident energy of a neutron then a of gamma-ray. The energy deposited in a scintillator by ionizing radiation is typically reported in electron-equivalent units, or MeV_{ee}. This allows one

to easily compare the scintillation yield of say alpha particles and protons using a single common unit. Kent State University [16] reported the proton light-response function for NE-213 given in Eq. (3.4).

For example, the NE-213 relative proton light-response function, converting proton kinetic energies T_p to electron-equivalent energies T_e, is given by

$$T_{\mathrm{e}} = -2.82 \cdot (1 - e^{(-0.25 \cdot T_p^{0.93})} + 0.83 \cdot T_p) \tag{3.4}$$

The proton light-response function of the Sjögren detector, Eq. (3.5), was measured to be 86% of the values reported by Kent State University. The Sjögren relative proton light-response function is given by

$$T_e = -2.43 \cdot (1 - e^{(-0.25 \cdot T_p^{0.93})} + 0.71 \cdot T_p). \tag{3.5}$$

In comparison, the NE-213 relative alpha particle light-response function for alpha particle kinetic energies T_α is given by

$$T_e = -5.90 \cdot (1 - e^{(-0.065 \cdot T_\alpha^{1.01})} + 0.41 \cdot T_\alpha). \tag{3.6}$$

Equations (3.4), (3.5) and (3.6) are shown in Fig. 3.11. Both the proton and alpha light-response functions are input parameters for the Stanton simulation as it considers both recoiling protons from (n,p) interactions and recoiling alphas from (n,^{12}c) interactions.

3.2.2 Typical output

The Stanton simulation output is a hypercube of neutron-detection efficiencies ε_n for different detector thresholds τ_n and neutron kinetic energies T_n as shown in Fig. 3.12. The surface output of Fig. 3.12 illustrates the general trend of high efficiency for low threshold setting and low neutron energy. The efficiency goes to zero as threshold and energy increase. This particular output is for a $5 \times 5 \times 5$ inch^3 detector but the general trend is shared by all the shapes investigated in this thesis.

By examining one detector-threshold setting at a time, insight into how the detection efficiency changes as a function of neutron kinetic energy in the region of interest (~0 — 70 MeV) may be obtained. The detection efficiency is the percentage of free neutrons passing through the detector that end up being detected. In Fig. 3.13, a slice from Fig. 3.12 at $\tau_n = 1.0$ MeV$_{ee}$ is shown. Such a detector-setting combination results in the detection of neutrons at down to 2 MeV. The detection efficiency peaks at 0.48 for

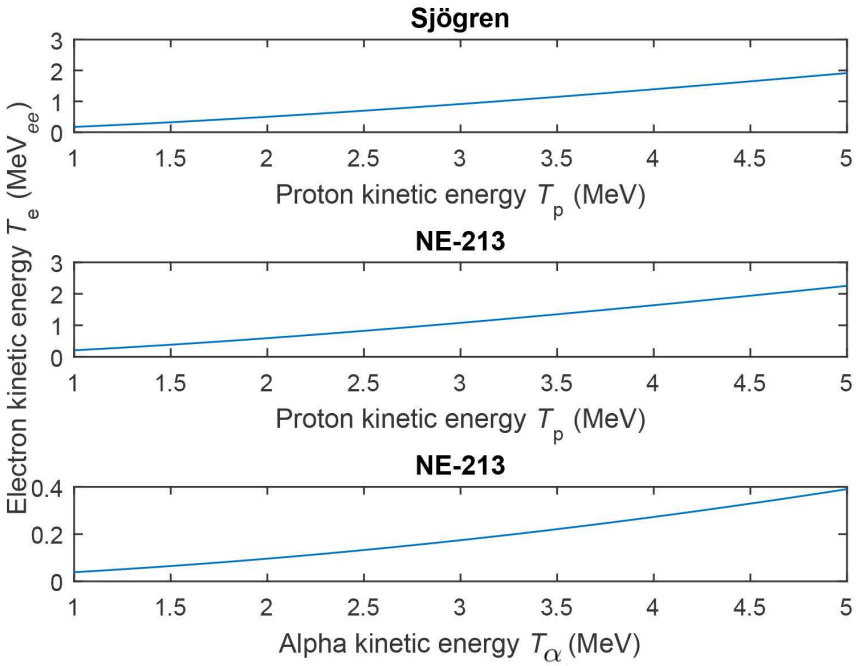

FIGURE 3.11: The NE-213 and Sjögren relative proton light-response functions and NE-213 alpha particle light-response functions. Sjögren only results in 86% of the light-response of the original NE-213. Alphas result in less than 20% electron kinetic energy per unit incoming energy, compared to protons.

6 MeV neutrons and decreases for higher energy neutrons down to a detection efficiency of ~0.25 at 70 MeV. The shape of this slice of the efficiency hypercube is representative of the behaviour of all detectors and all thresholds and comes from the decreasing cross sections of free neutron interactions with increasing energy.

3.3 Two-body Kinematics

Photons of energy E_γ incident upon the targets of Al, Cu or Fe can knock a neutron out, resulting in a free neutron with an energy E_n. Calculating the kinematics of this reaction gives the exact E_n for different E_γ and angles of knocked-out neutrons. This allows the detection efficiency as a function of neutron energy to be mapped into the detection efficiency as a function of beam energy. Since the beam is tagged, it is then a straightforward matter to determine the detection efficiency approporiate for the analysis of the energy bin in question.

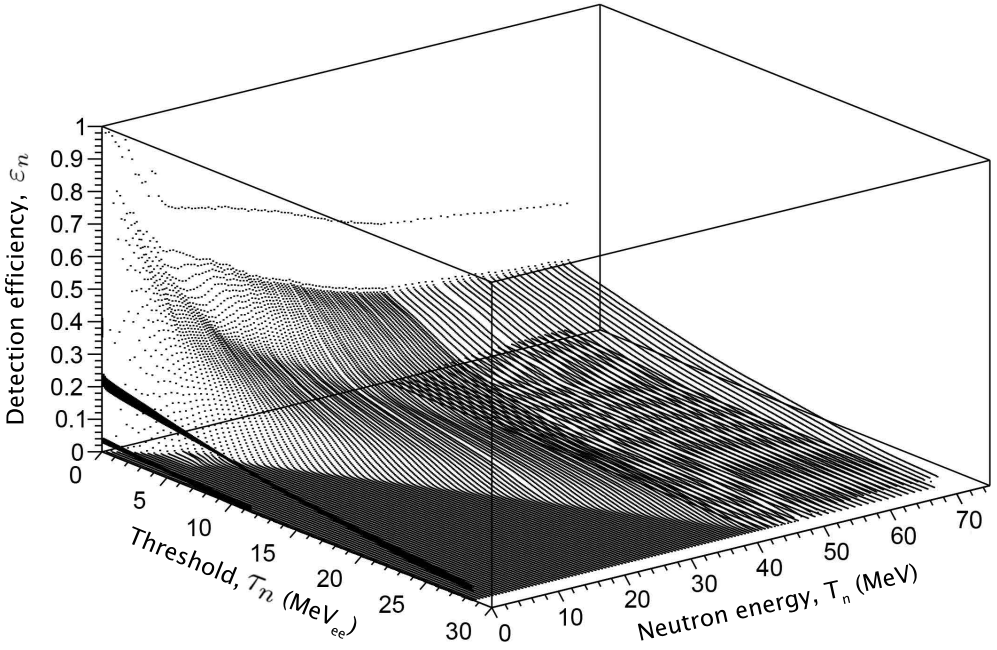

FIGURE 3.12: Typical output from the Stanton simulation. This particular hypercube is for a $5 \times 5 \times 5$ inch^3 NE-213 detector. The detection efficiency peaks for low threshold values and low neutron energies. At $\tau_n = 30$ MeV$_{ee}$ and $T_n = 70$ MeV, no neutrons are detected, $\varepsilon_n = 0$.

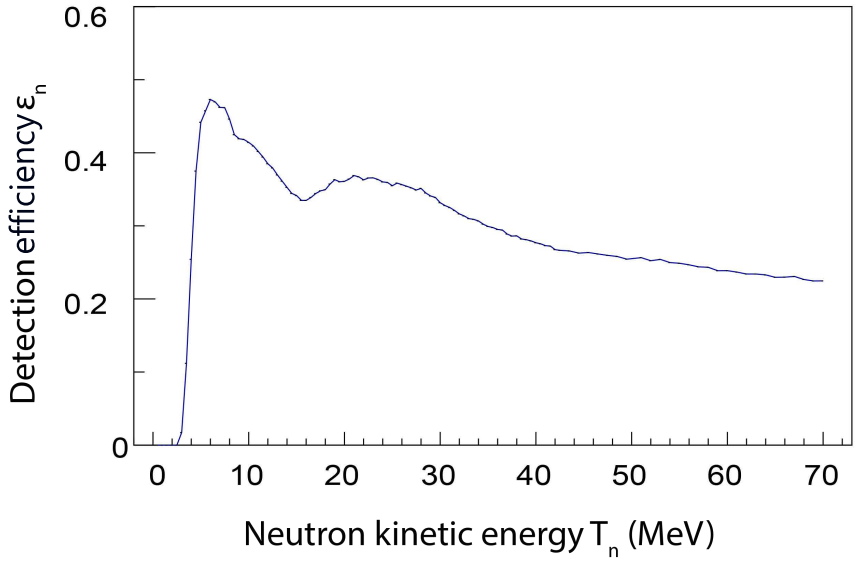

FIGURE 3.13: The neutron-detection efficiency reported by the Stanton simulation for a $5 \times 5 \times 5$ inch^3 NE-213 detector. Neutron kinetic energies are simulated up to 70 MeV and the detector-threshold is set to 1.0 MeV$_{ee}$. The lowest detectable energy neutrons are at 3 MeV. The highest efficiency is for 6 MeV neutrons of which 47% are detected. Above 30 MeV, the efficiency has a plateau of ~0.25 on to 70 MeV.

3.3.1 Elastic Neutron Photo-knockout

Neutrons can be knocked out of nuclei via elastic collision with photons, as shown in Fig. 3.14. An incoming photon with energy E_γ and momentum p_γ interacts with a target nucleus T, knocking out a neutron with energy E_n and momentum p_n at an angle θ with respect to the incident direction of the photon. The particle R, recoiling at an angle φ, is the former nucleus T in its ground state, minus its missing neutron. By applying the conservation of momentum and energy to the above situation, it is possible to calculate the kinetic energy of the freed neutrons as a function of angle for any given incident photon energy. See Appendix D for details and Table 3.3 for a summary of results.

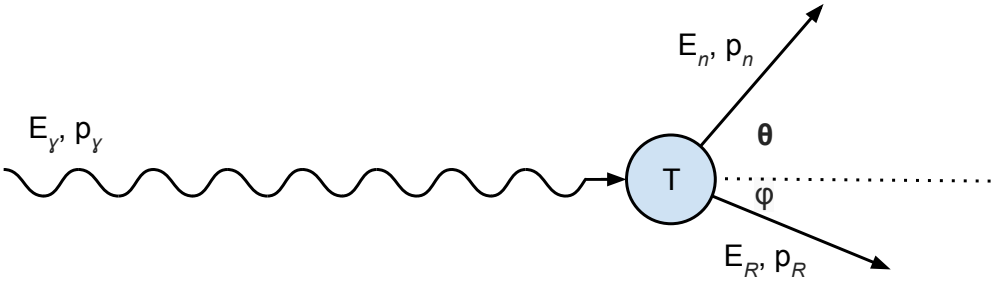

FIGURE 3.14: A two-body photo-knockout reaction where an incoming photon interacts with a target nucleus T, knocking out a neutron n, and leaving recoil particle R in its ground state.

3.3.2 Photon/Neutron Energy Correspondence

Using the method explained in Section 3.3.1, the photon-beam energies have been translated into corresponding elastic knockout neutron energies for the targets that were used, see Fig. 3.15. Recall from Table 2.1 that the incident beam photons have energies between 2.40 MeV to 66.31 MeV.

As shown in Fig. 3.15, the photon-neutron correspondence between the ^{56}Fe and ^{63}Cu targets are very similar (with a difference of ~0.10 MeV) and coincide as the upper line. The lowest energy photons knocking out neutrons are seen at 12.73 MeV for ^{27}Al, 10.87 MeV for ^{56}Fe and 10.90 MeV for ^{63}Cu. Elastic knockout neutrons are thus kinematically prohibited for photon beam energies lower than ~10.9 MeV. The first bin of the hodoscope corresponds to photon beam energies up to 10 MeV and will not have knocked out any neutrons. The photon energies of all the bins for neutrons knocked out at 90° to the incident beam are presented in Table 3.3. The kinetic energies of the neutrons vary between 0 MeV to 55 MeV and are representative of the data from 45° and 135° angles as well. Neutrons knocked out at 135° are ~1% lower in energy and

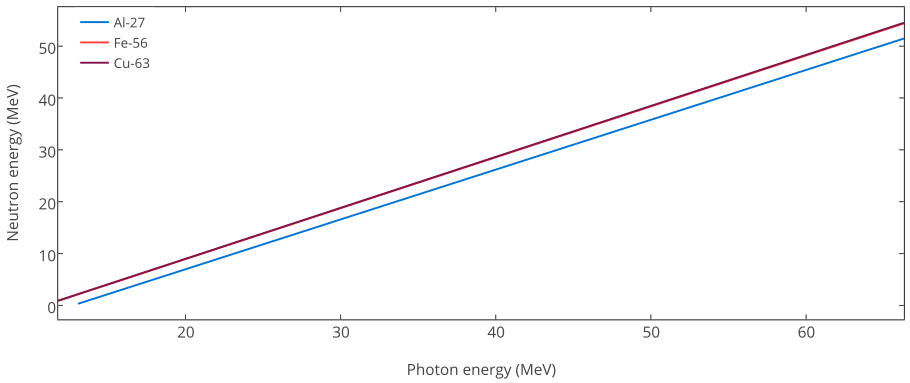

FIGURE 3.15: The energy of the elastic knockout neutrons at 90° of the incident beam as a function of incident photons for Al, Fe and Cu. The Fe and Cu data overlap as the upper line. The neutron energy inceases with higher photon energy and forward angle. Straight forward knockout, at 0°, would result in the highest energy neutrons.

knockout at 45° are ~1% higher. See Appendix D for a complete list of the kinematical calculations for all photon beam bins, neutron angles and targets.

TABLE 3.3: Photon and neutron energies for the 90° Nordball array.

Bin	Photon energy (MeV)	Neutron energy (MeV)		
		^{27}Al	^{56}Fe	^{63}Cu
1	9.19	-	-	-
2	19.26	6.28	8.23	8.25
3	28.50	15.16	17.30	17.34
4	37.04	23.37	25.68	25.74
5	45.01	31.02	33.50	33.57
6	52.49	38.21	40.84	40.92
7	59.57	45.00	47.78	47.88
8	66.31	51.46	54.38	54.50

3.4 Simulation Results

3.4.1 Cross sections

The energy region of interest in this investigation is that where the (γ, n) cross section is the largest. For our aluminum, steel and copper targets, the most common isotopes are ^{27}Al, ^{56}Fe and ^{63}Cu. The IAEA Photonuclear Data Library [17] offers recommended cross sections for these nuclei, see Fig. 3.16. Using the calulations described in Appendix D for each of the isotopes mentioned above and assuming single neutron

knockout, the cross sections as a function of incident photon energies can be mapped into cross sections as a function of outgoing neutron kinetic energies, see Fig. 3.17.

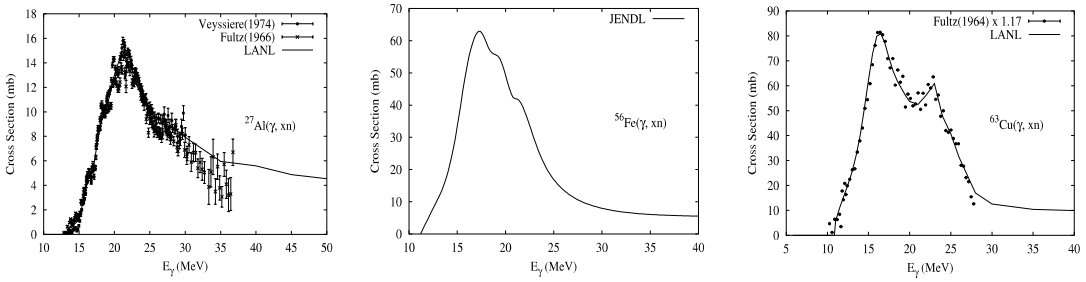

FIGURE 3.16: Cross sections for the ^{27}Al(γ, xn), ^{56}Fe(γ, xn) and ^{63}Cu(γ, xn) reactions [17]. xn means there is at least one neutron in the final state. ^{27}Al has the lowest cross section of the three and ^{63}Cu the highest. JENDL is the Japanese Evaluated Nuclear Data Library (http://wwwndc.jaea.go.jp/jendl/j40/j40.html). LANL is the Los Alamos National Laboratory(http://www.lanl.gov/).

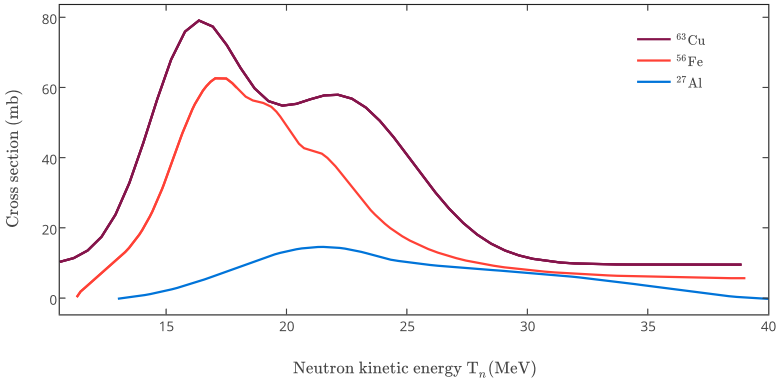

FIGURE 3.17: The ^{27}Al, ^{56}Fe and ^{63}Cu cross sections plotted against neutron kinetic energy. The purple line represents ^{63}Cu, which has the highest cross section of the three. The red, ^{56}Fe, peaks at 17 MeV. The blue line represents ^{63}Cu which peaks for neutrons with 22 MeV and has a more flat distribution than the other two.

Armed with the knowlege of the neutron kinetic energy regions corresponding to the target cross sections for neutron knockout, the next step was to compare with the Stanton-simulated neutron-detection efficiency. Figure 3.18 illustrates a comparison between the neutron-detection efficiency predicted by the Stanton simulation for the NE-213 cup for eight different detector threshold settings and the three targets of interest. The efficiency curves show edges rising to a maximum efficiency and then flattening out for higher energies. The simulated thresholds, τ_n, are between 1.0 MeV$_{ee}$ and 4.5 MeV$_{ee}$. As the threshold increases, efficiency decreases. The maximum efficiency decreases from ~0.28 for $\tau_n = 1.0$ MeV$_{ee}$ to ~0.09 for $\tau_n = 4.5$ MeV$_{ee}$. The lowest energy of neutrons that are

detectable increases with increasing threshold. Neutrons of ~1.5 MeV can be detected with $\tau_n = 1.0$ MeV$_{ee}$, whereas the lowest detectable energy neutrons at $\tau_n = 4.5$ MeV$_{ee}$ are ~8.0 MeV. The overlayed ^{27}Al, ^{56}Fe and ^{63}Cu (γ,n) cross sections are the region of highest interest to detect. The photo-tagging bins 2 and 3 correspond to photoknockout neutron energies from 0 MeV to ~17 MeV. Bin 2 and 3 have been marked in color and match the region of interst well. Bin 1, which does not correspond to any photoknockout neutrons, can be disregarded. With $\tau_n = 1.0$ MeV$_{ee}$ the majority of the photoknockout neutrons can be detected. The peak at the center of bin 2 corresponds with the peaks of ^{56}Fe and ^{63}Cu. Bin 3 covers more of the ^{27}Al photoknockout neutrons. For higher threshold settings, bin 3 has a flatter neutron-detection efficiency curve. By dividing the yields by these simulated neutron-detection efficiencies according to Eq. (3.3), the true number of photoknockout neutrons can be obtained. Corresponding Figures for the Nordball and Sjgren detectors can be seen in Appendix E. Their larger volumes result in higher neutron-detection efficiencies of up to 0.58. The general shape of the simulated neutron-detection efficiencies however, is similar to that of the smaller NE-213 cup.

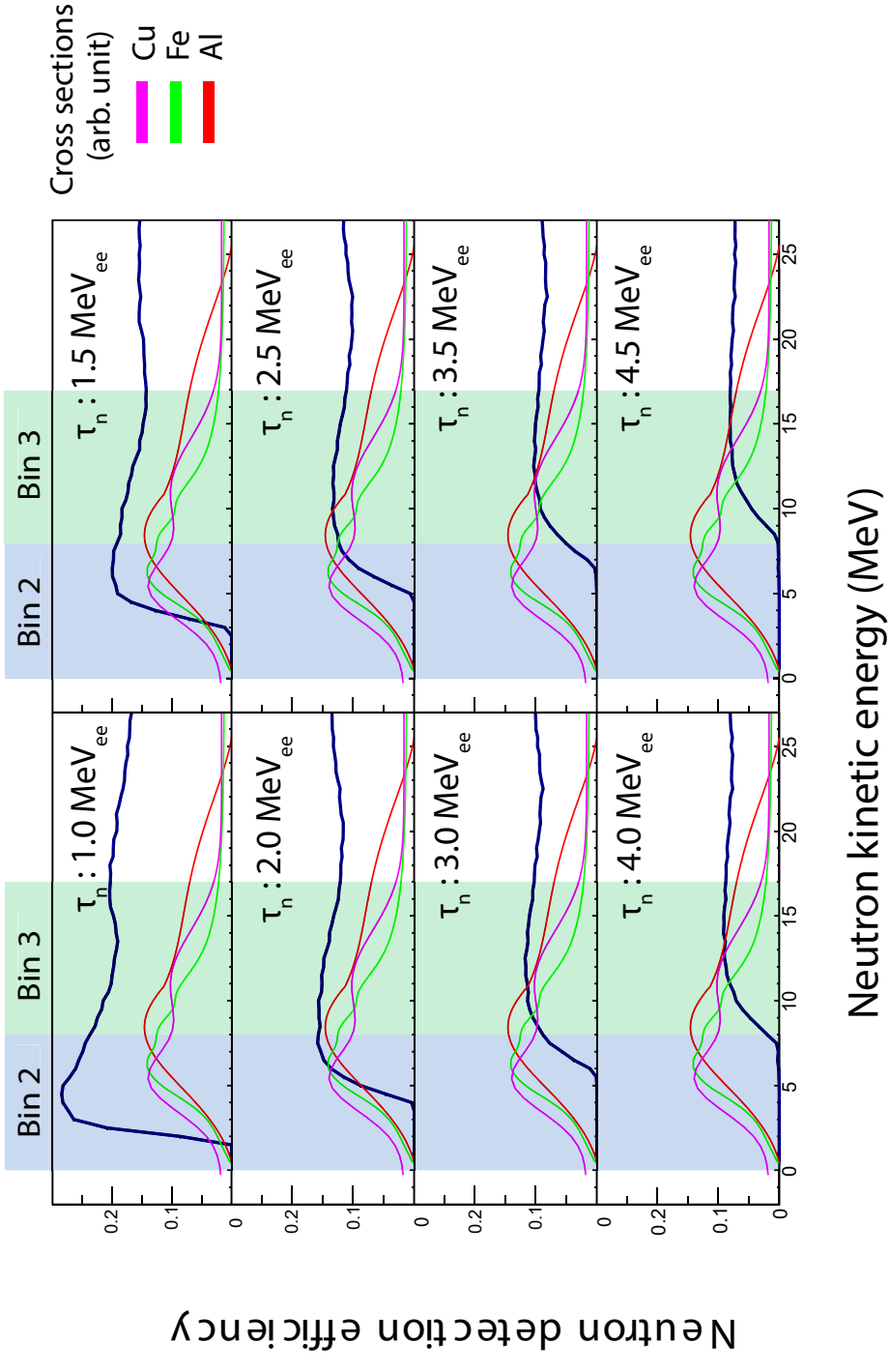

FIGURE 3.18: The detection efficiency of the NE-213 cup detector for 8 different detector threshold settings together with overlaid photoknockout cross sections for ^{27}Al, ^{56}Fe and ^{63}Cu, in red, green and purple respectively. The neutron energies corresponding to photon-energy bins 2 (9.85 — 19.86 MeV) and 3 (19.86 — 29.05 MeV are shown as well. The simulated detection efficiency is the thick blue line. The threshold τ_n is set between 1.5 — 5.0 MeV$_{ee}$.

Chapter 4

Conclusion

The purpose of this project was to investigate fast photoneutron production from a series of materials commonly used for backing thermal-neutron beam guides. At a neutron spallation source, these materials get exposed to high-energy gamma-rays coming from the spallation target and moderator. These high-energy gamma-rays interact with the backing materials, spraying unwanted fast neutrons into the experimental endstations. The idea was to create well-defined experimental geometries where the probability for fast-neutron photoproduction could be precisely measured. By comparing the data obtained to careful simulations performed using multiple software packages, tuned exactly to the experimental setup, validation benchmarks can be obtained. Simulation validation benchmarks are important because they establish the believability of the software efforts.

4.1 This work

In this, the first step of the project, fast photo-neutron knockout measurements were successfully performed using the photon-tagging facility at MAX-lab. Precision beams of high-energy photons were used to knock out fast neutrons from targets of aluminium, copper and steel. These targets are common materials used for backing thermal-neutron beam guides. Organic liquid scintillator detectors placed at different angles around the targets were used to detect the knocked-out photoneutrons. Interactions between the neutrons and the organic liquid scintillators resulted in scintillations which were registered with PMTs. The liquid-scintillator detectors were energy-calibrated using the well-understood gamma-ray sources ThC and Am/Be. These sources have Compton edges at 2.24 MeV and 4.20 MeV respectively. These edges were localized using the method first suggested by H. H. Knox [10]. The energy calibrations were then applied to

the source spectra to establish the hardware measurement thresholds. These hardware thresholds are the lowest limits in energy deposited in the scintillators, under which no events are registered. The hardware thresholds were reported in the unit MeV_{ee}. This electron-equivalent energy unit describes how much energy the recoiling atomic electrons deposit in the scintillator medium, rather than how much energy the incoming particle (in this case, gamma-ray) had. It is useful because it provides a neutral baseline which allows scintillation yields from different particle types to be compared.

The hardware thresholds were then used as input to an absolute neutron-detection efficiency Monte Carlo simulation known as STANTON to establish the best-case neutron-detection efficiency achieved in the measurement. The neutron-detection efficiency curves were strong functions of the applied light-yield threshold, and tended towards step functions, with the step occurring at the neutron-energy threshold. The thresholds were then systematically increased in software to study the reduction in detection efficiency as a function of the increase in applied light-yield threshold. Higher light-yield thresholds resulted in flatter neutron detection-efficiency curves with higher neutron-energy thresholds and lower overall efficiency.

This study was useful as it provided guidance in the data analysis of the neutron yield as to where to optimally set the applied light-yield detector threshold in software. Too low a threshold means higher detection-efficiency but the events of interest may be lost in a flood of uninteresting low-energy background. Too high a threshold means lower background but events of interest may be cut away. Knowledge of the tradeoff between the applied light-yield detector threshold (which directly affects the neutron-energy threshold and thus the identified neutron yield) and the neutron-detection efficiency will allow for a minimal uncertainty extraction of the cross section from the data.

4.2 Looking forward

The next step in this project will be the determination of the neutron yield as a function of applied light-yield detector threshold. Studying tradeoff between neutron yield and applied light-yield threshold (that is, detection efficiency) with an eye on minimizing the uncertainty in the cross section will allow for an optimization of the procedure. Recall that the cross section is proportional to the quotient of the neutron yield and the detection efficiency. Once the optimum applied light-yield threshold is determined, the neutron yield may be extracted, normalized to the neutron-detection efficiency and other variables such as solid angle, target thickness and incident photon-beam flux, and compared to existing results. At this point detailed efforts to precisely simulate the experiment using comprehensive, industry-standard toolkits such as GEANT4 [11] and

MCNPX [18] will commence. The tasks listed in this section are beyond the scope of this thesis and are listed here only for the sake of completeness.

4.3 Suggestions for improvement

Looking back over the project, it is clear that some improvements could be made.

- The detectors connected to a newer high voltage power supply were more stable over time, producing more consistent results. The old LeCroy high voltage power supply is starting to show its age and should be replaced.
- The STANTON simulation package lacked documentation and would have been much easier to understand and use with a short read-me guide.
- For future students doing similar work - if you are not already familiar with ROOT or C++, I would suggest exporting the data to a program you are familiar with. Becoming sufficiently familiar with ROOT and C++ to perform data analysis required a substantial investment of time.

Appendix A

Contribution of the Author

Table A.1: A summary of the contribution of the author to this project.

Month	Activity
Oct 2014	Background reading, Jefferson Lab DOE Radiation Worker 1 DNPLU walkthrough, performed measurements of Appendix F
Nov 2014	Background reading, performed experiments at MAX-lab
Dec 2014	Background reading, undergraduate supervision, set up ROOT programs
Mar 2015	Data analysis
April 2015	Data analysis, writing of thesis
May 2015	Writing of thesis
June - Aug 2015	Building and testing of ^{10}B neutron detector
Nov - Dec 2015	Writing of thesis

Appendix B

Self Reflection

For periods spread over more than a year, interrupted by internships in both Kazakhstan and Belgium, I have been part of a group investigating fast photoneutrons. My tasks have been varying, interesting and challenging. Some challenges, especially in the starting phase, arose from the fact that I have not taken any courses on nuclear physics previous to this project. With the excellent help from the collegaues I have gotten to work with and much reading, the challenges were overcome. I am now looking forward to digging deeper into the world of neutrons through a PhD position.

Appendix C

Detector Energy Calibration Data

TABLE C.1: The calibration functions determined using the Knox method for all the detectors and the four calibration dates.

hvq	Detector	Channel number = k · MeV + m							
		24-Nov		01-Dec		08-Dec		15-Dec	
		k	m	k	m	k	m	k	m
hvq 0	Nb, pen	256.33	164.07	-	-	-	-	269.43	164.29
hvq 1	Nb, pen	212.31	205.42	-	-	204.35	208.38	208.13	208.19
hvq 2	Nb, hex	199.01	185.14	-	-	195.11	190.70	-	-
hvq 3	Nb, pen	177.22	215.56	-	-	179.79	212.68	178.82	213.27
hvq 5	Nb, hex	262.46	152.06	274.67	161.89	300.02	151.88	300.13	154.14
hvq 6	Nb, hex	188.69	168.61	185.96	167.95	185.03	166.32	185.01	167.67
hvq 7	Nb, hex	190.37	223.20	190.38	222.57	192.52	219.52	192.89	218.25
hvq 9	Nb, hex	217.69	168.36	209.84	174.69	213.78	170.33	214.23	171.47
hvq 10	Nb, hex	189.61	189.29	188.74	189.24	191.36	186.56	190.35	188.19
hvq 11	Nb, pen	198.35	171.36	194.39	172.42	196.30	169.71	195.88	170.77
hvq 12	EJ-305 cup	236.30	211.94	274.77	193.52	276.23	202.00	277.43	186.80
hvq 13	NE-213 cup	231.16	142.45	221.20	151.01	214.52	170.33	208.85	157.46
hvq 15	NE-213 Sjögren	228.49	163.16	231.97	198.78	228.60	180.84	235.13	203.67

Appendix D

Photon To Neutron Energy Conversion

TABLE D.1: The photon-tagger settings with channels, recoil post-bremsstrahlung electron energies and corresponding photon energies.

Channel	E_{recoil} (MeV)	E_γ (MeV)	Channel	E_{recoil} (MeV)	E_γ (MeV)	Channel	E_{recoil} (MeV)	E_γ (MeV)
1	98.39	66.31	22	116.83	47.87	43	138.44	26.26
2	99.22	65.48	23	117.78	46.92	44	139.58	25.12
3	100.05	64.65	24	118.73	45.97	45	140.73	23.97
4	100.88	63.82	25	119.69	45.01	46	141.89	22.81
5	101.72	62.98	26	120.66	44.04	47	143.06	21.64
6	102.56	62.14	27	121.64	43.06	48	144.24	20.46
7	103.41	61.29	28	122.62	42.08	49	145.44	19.26
8	104.27	60.43	29	123.61	41.09	50	146.65	18.05
9	105.13	59.57	30	124.61	40.09	51	147.87	16.83
10	105.99	58.71	31	125.62	39.08	52	149.11	15.59
11	106.86	57.84	32	126.63	38.07	53	150.36	14.34
12	107.74	56.96	33	127.66	37.04	54	151.63	13.07
13	108.62	56.08	34	128.69	36.01	55	152.91	11.79
14	109.51	55.19	35	129.74	34.96	56	154.20	10.50
15	110.40	54.30	36	130.79	33.91	57	155.51	9.19
16	111.30	53.40	37	131.85	32.85	58	156.84	7.86
17	112.21	52.49	38	132.92	31.78	59	158.18	6.52
18	113.12	51.58	39	134.01	30.69	60	159.53	5.17
19	114.04	50.66	40	135.10	29.60	61	160.91	3.79
20	114.96	49.74	41	136.20	28.50	62	162.30	2.40
21	115.90	48.80	42	137.32	27.38			

D.1 Neutron energies via two body photoknockout

The reaction is shown in Fig. 3.14. An incoming photon with energy E_γ and momentum p_γ interacts with a target nucleus T which loses a neutron with energy E_n and momentum p_n at an angle θ from the incident direction of the photon. The recoil particle R, going at an angle φ is the former nucleus T minus its missing neutron.

The calculations below are standard and reproduced with permission [19]. Through the conservation of momentum and energy, it is possible to calculate the kinetic energy of the photoknockout neutrons. The recoil particle R is assumed to carry no extra energy from the photon as an excitation. Then all the remaining energy of the photon becomes kinetic energy and the conservation of momentum implies

$$p_\gamma = p_\mathrm{n}\cos\theta + p_\mathrm{R}\cos\varphi \tag{D.1}$$

$$0 = p_n\cos\theta - p_R\sin\varphi. \tag{D.2}$$

Solving Eqs. (D.1) and (D.2) for cosφ and sinφ respectively, squaring and adding them together and using the trigonometric identity $\sin^2\varphi + \cos^2\varphi = 1$ will yield

$$p_R^2 = p_n^2 + E_\gamma^2 - 2p_nE_\gamma\cos\theta. \tag{D.3}$$

The total energy must be the same before and after the interaction

$$E_\gamma + E_T = E_n + E_R. \tag{D.4}$$

Solving Eq. (D.4) for the energy of the recoiling particle and squaring it gives

$$E_R^2 = E_\gamma^2 + E_T^2 + E_n^2 + 2E_\gamma E_T - 2E_\gamma E_n - 2E_T E_n. \tag{D.5}$$

We can substitute the energy of the recoil particle as $E_R^2 = p_R^2 + m_B^2$. Equation D.5 thus becomes

$$p_R^2 = E_\gamma^2 + E_T^2 + E_n^2 + 2E_\gamma E_T - 2E_\gamma E_n - 2E_T E_n - m_R^2. \tag{D.6}$$

A comparison of Eqs. D.3 and D.6 and the fact that the target is at rest ($E_T = m_T$) result in

$$p_n^2 - 2p_nE_\gamma\cos\theta = m_T^2 + E_n^2 + 2E_\gamma m_T - 2E_\gamma E_n - 2E_n m_T - m_R^2. \tag{D.7}$$

Finally, $p_n^2 = E_n^2 - m_n^2$, so that

$$E_n^2 - m_n^2 - 2sqrtE_n^2 - m_n^2 E_\gamma \cos\theta = m_T^2 + E_n^2 + 2E_\gamma m_T - 2E_\gamma E_n - 2E_n m_T - m_R^2. \quad \text{(D.8)}$$

To solve equation D.8, define the quantities

$$M^2 = m_R^2 - m_n^2 - m_T^2, \quad \text{(D.9)}$$

$$E_0 = E_\gamma + m_T. \quad \text{(D.10)}$$

Squaring Eq. D.8 and rewriting in terms of the above quantities produces a quadratic equation in E_n

$$\begin{gathered}\{4[E_\gamma^2(\cos\theta)^2 - E_0^2]\}E_n^2 + \\ \{4E_0[2E_\gamma m_T - M^2]\}E_n + \\ \{4E_\gamma[m_T(M^2 - E_\gamma m_T) - E_\gamma(\cos\theta)^2 m_n^2] - M^4\} = 0. \quad \text{(D.11)}\end{gathered}$$

By defining the following variables

$$a = 4[E_\gamma^2(\cos\theta)^2 - E_0^2, \quad \text{(D.12)}$$

$$b = 4E_o[2E_\gamma m_T - M^2], \quad \text{(D.13)}$$

$$c = 4E_\gamma[m_T(M^2 - E_\gamma m_T) - E_\gamma(\cos\theta)^2 m_n^2] - M^4, \quad \text{(D.14)}$$

the solution to Eq. D.1 will be given by

$$E_n = \frac{1}{2a}[-b \pm \sqrt{b^2 - 4ac}]. \quad \text{(D.15)}$$

Only one of the two solutions to Eq. D.15 is physical. The kinetic energy of the neutron, T_n, is thus given by

$$T_n = E_n^{\text{physical}} - m_n. \quad \text{(D.16)}$$

The quadratic Eq (D.1) can easily be solved. Knowledge of the energy of the incident photon, the mass of the target nucleus (Al, Fe or Cu), the mass of the detected particle (the neutron), the angle θ at which the neutron is detected (where the detectors were placed) and the mass of the recoiling nucleus R are required.

TABLE D.2: Photon and corresponding neutron energies in MeV, channels 1 — 30.

Channel	Photon energy (MeV)	Neutron energy (MeV)								
		^{27}Al			^{56}Fe			^{63}Cu		
		43.5°	88.4°	132.7°	43.5°	88.4°	132.7°	43.5°	88.4°	132.7°
1	66.31	52.04	51.46	50.87	54.67	54.38	54.09	54.75	54.50	54.24
2	65.48	51.24	50.67	50.09	53.85	53.57	53.29	53.94	53.69	53.43
3	64.65	50.43	49.87	49.31	53.03	52.76	52.48	53.12	52.87	52.62
4	63.82	49.62	49.07	48.52	52.21	51.94	51.67	52.29	52.05	51.81
5	62.98	48.80	48.27	47.73	51.38	51.12	50.85	51.46	51.23	50.99
6	62.14	47.98	47.46	46.93	50.55	50.29	50.03	50.63	50.40	50.17
7	61.29	47.15	46.64	46.13	49.71	49.46	49.20	49.79	49.56	49.34
8	60.43	46.32	45.82	45.32	48.87	48.62	48.37	48.95	48.73	48.50
9	59.57	45.49	45.00	44.51	48.02	47.78	47.53	48.10	47.88	47.66
10	58.71	44.64	44.17	43.69	47.17	46.93	46.69	47.24	47.03	46.82
11	57.84	43.80	43.33	42.87	46.31	46.08	45.84	46.38	46.18	45.97
12	56.96	42.95	42.49	42.04	45.44	45.22	44.99	45.52	45.31	45.11
13	56.08	42.09	41.65	41.20	44.57	44.35	44.13	44.64	44.45	44.25
14	55.19	41.22	40.79	40.36	43.70	43.48	43.27	43.77	43.58	43.38
15	54.30	40.36	39.94	39.52	42.82	42.61	42.40	42.88	42.70	42.51
16	53.40	39.48	39.07	38.67	41.93	41.72	41.52	41.99	41.81	41.63
17	52.49	38.60	38.21	37.81	41.03	40.84	40.64	41.10	40.92	40.75
18	51.58	37.71	37.33	36.95	40.13	39.94	39.75	40.20	40.03	39.86
19	50.66	36.82	36.45	36.07	39.23	39.04	38.85	39.29	39.13	38.96
20	49.74	35.92	35.56	35.20	38.32	38.13	37.95	38.38	38.22	38.05
21	48.80	35.02	34.67	34.32	37.40	37.22	37.05	37.46	37.30	37.14
22	47.87	34.10	33.77	33.43	36.47	36.30	36.13	36.53	36.38	36.23
23	46.92	33.18	32.86	32.53	35.54	35.37	35.21	35.59	35.45	35.30
24	45.97	32.26	31.94	31.63	34.60	34.44	34.28	34.65	34.51	34.37
25	45.01	31.33	31.02	30.72	33.65	33.50	33.34	33.70	33.57	33.43
26	44.04	30.39	30.09	29.80	32.70	32.55	32.40	32.75	32.62	32.49
27	43.06	29.44	29.16	28.87	31.73	31.59	31.45	31.79	31.66	31.53
28	42.08	28.48	28.21	27.94	30.76	30.63	30.49	30.81	30.69	30.57
29	41.09	27.52	27.26	27.00	29.79	29.66	29.52	29.83	29.72	29.60
30	40.09	26.55	26.30	26.05	28.80	28.68	28.55	28.85	28.74	28.62

Table D.3: Photon and corresponding neutron energies in MeV, channels 31 — 62.

Channel	Photon energy (MeV)	Neutron energy (MeV)								
		^{27}Al			^{56}Fe			^{63}Cu		
		43.5°	88.4°	132.7°	43.5°	88.4°	132.7°	43.5°	88.4°	132.7°
31	39.08	25.57	25.33	25.09	27.81	27.69	27.57	27.85	27.75	27.64
32	38.07	24.58	24.36	24.13	26.81	26.69	26.57	26.85	26.75	26.64
33	37.04	23.59	23.37	23.15	25.79	25.68	25.57	25.84	25.74	25.64
34	36.01	22.58	22.38	22.17	24.77	24.67	24.56	24.81	24.72	24.63
35	34.96	21.57	21.37	21.18	23.75	23.65	23.55	23.78	23.70	23.61
36	33.91	20.55	20.36	20.18	22.71	22.61	22.52	22.74	22.66	22.58
37	32.85	19.52	19.34	19.17	21.66	21.57	21.48	21.70	21.62	21.54
38	31.78	18.48	18.31	18.15	20.60	20.52	20.43	20.64	20.56	20.49
39	30.69	17.43	17.27	17.12	19.54	19.46	19.38	19.57	19.50	19.43
40	29.60	16.37	16.22	16.08	18.46	18.38	18.31	18.49	18.42	18.36
41	28.50	15.29	15.16	15.03	17.37	17.30	17.23	17.40	17.34	17.28
42	27.38	14.21	14.09	13.96	16.27	16.21	16.14	16.30	16.24	16.18
43	26.26	13.12	13.01	12.89	15.16	15.10	15.04	15.19	15.14	15.08
44	25.12	12.02	11.91	11.81	14.04	13.99	13.93	14.07	14.02	13.97
45	23.97	10.91	10.81	10.71	12.91	12.86	12.81	12.93	12.89	12.84
46	22.81	9.78	9.69	9.61	11.77	11.72	11.68	11.79	11.75	11.71
47	21.64	8.64	8.57	8.49	10.61	10.57	10.53	10.63	10.59	10.56
48	20.46	7.50	7.43	7.36	9.45	9.41	9.37	9.46	9.43	9.40
49	19.26	6.33	6.28	6.22	8.27	8.23	8.20	8.28	8.25	8.22
50	18.05	5.16	5.11	5.06	7.07	7.05	7.02	7.09	7.06	7.04
51	16.83	3.98	3.93	3.89	5.87	5.85	5.82	5.88	5.86	5.84
52	15.59	2.78	2.74	2.71	4.65	4.63	4.61	4.66	4.64	4.62
53	14.34	1.56	1.54	1.52	3.42	3.40	3.39	3.42	3.41	3.40
54	13.07	0.33	0.32	0.31	2.17	2.16	2.15	2.18	2.17	2.16
55	11.79	-	-	-	0.91	0.90	0.90	0.91	0.91	0.90
56	10.50	-	-	-	-	-	-	-	-	-
57	9.19	-	-	-	-	-	-	-	-	-
58	7.86	-	-	-	-	-	-	-	-	-
59	6.52	-	-	-	-	-	-	-	-	-
60	5.17	-	-	-	-	-	-	-	-	-
61	3.79	-	-	-	-	-	-	-	-	-
62	2.40	-	-	-	-	-	-	-	-	-

Appendix E

Stanton Simulated Neutron Detection Efficiencies

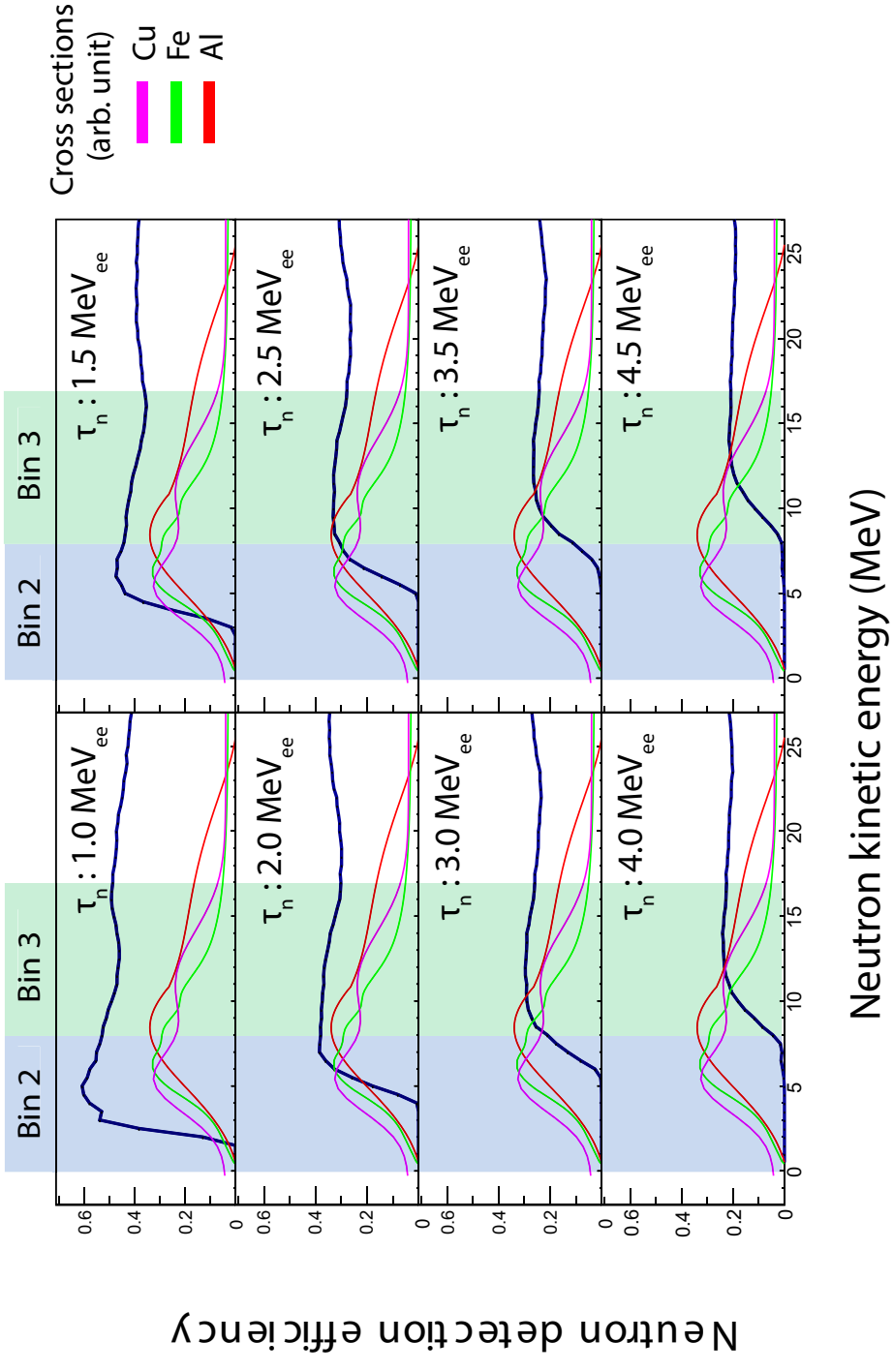

FIGURE E.1: The detection efficiency of the NE213 Sjögren detector for 8 different detector threshold settings together with overlaid photoknockout cross sections for ^{27}Al, ^{56}Fe and ^{63}Cu, in red, green and purple respectively. The neutron energies corresponding to photon-energy bins 2 (9.85 — 19.86 MeV) and 3 (19.86 — 29.05 MeV are shown as well. The simulated detection efficiency is the thick blue line. The threshold τ_n is set between 1.5 — 5.0 MeV$_{ee}$.

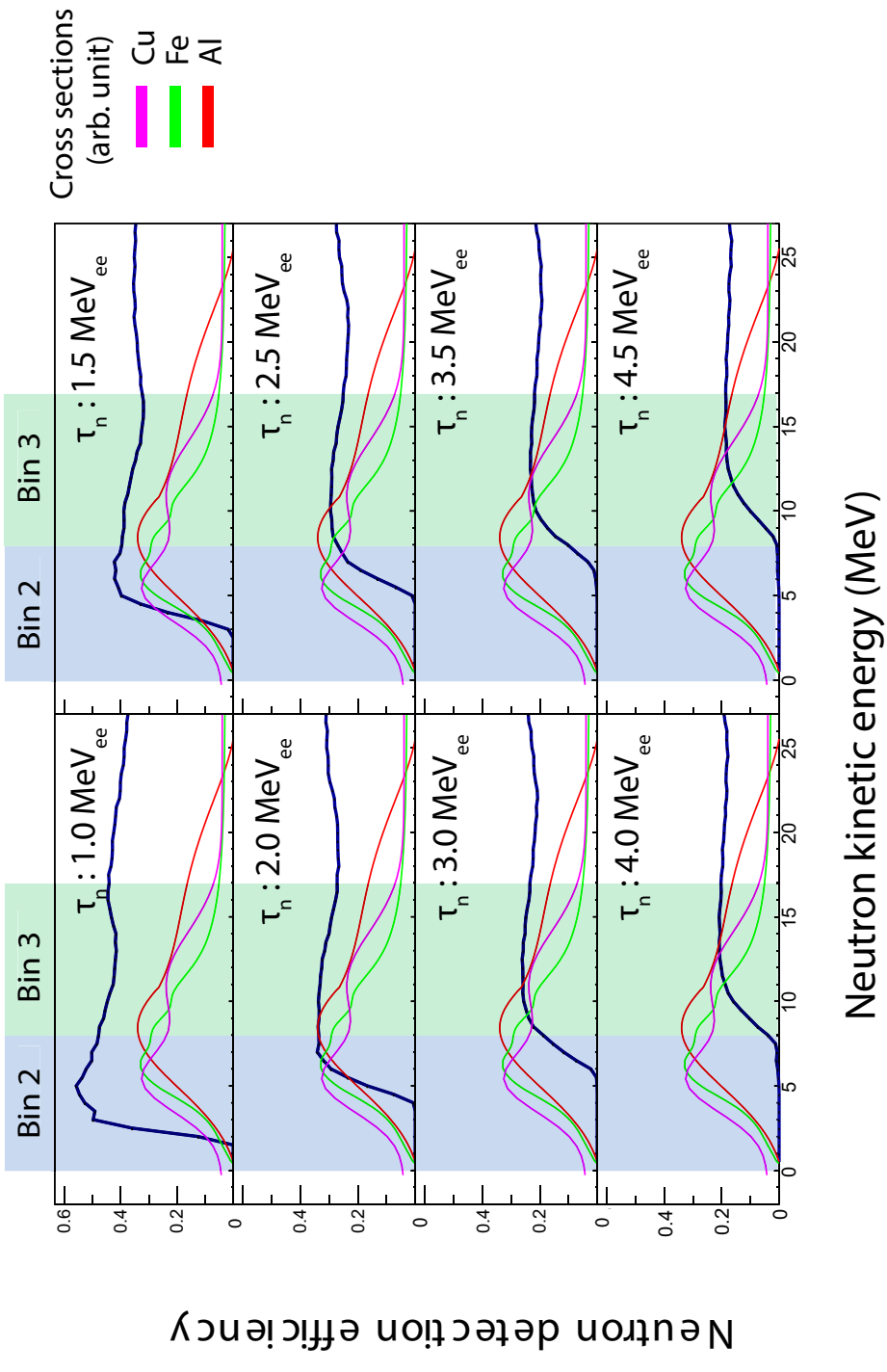

FIGURE E.2: The detection efficiency of the hexagonal Nordball detector for 8 different detector threshold settings together with overlaid photoknockout cross sections for ^{27}Al, ^{56}Fe and ^{63}Cu, in red, green and purple respectively. The neutron energies corresponding to photon-energy bins 2 (9.85 — 19.86 MeV) and 3 (19.86 — 29.05 MeV are shown as well. The simulated detection efficiency is the thick blue line. The threshold τ_n is set between 1.5 — 5.0 MeV$_{ee}$.

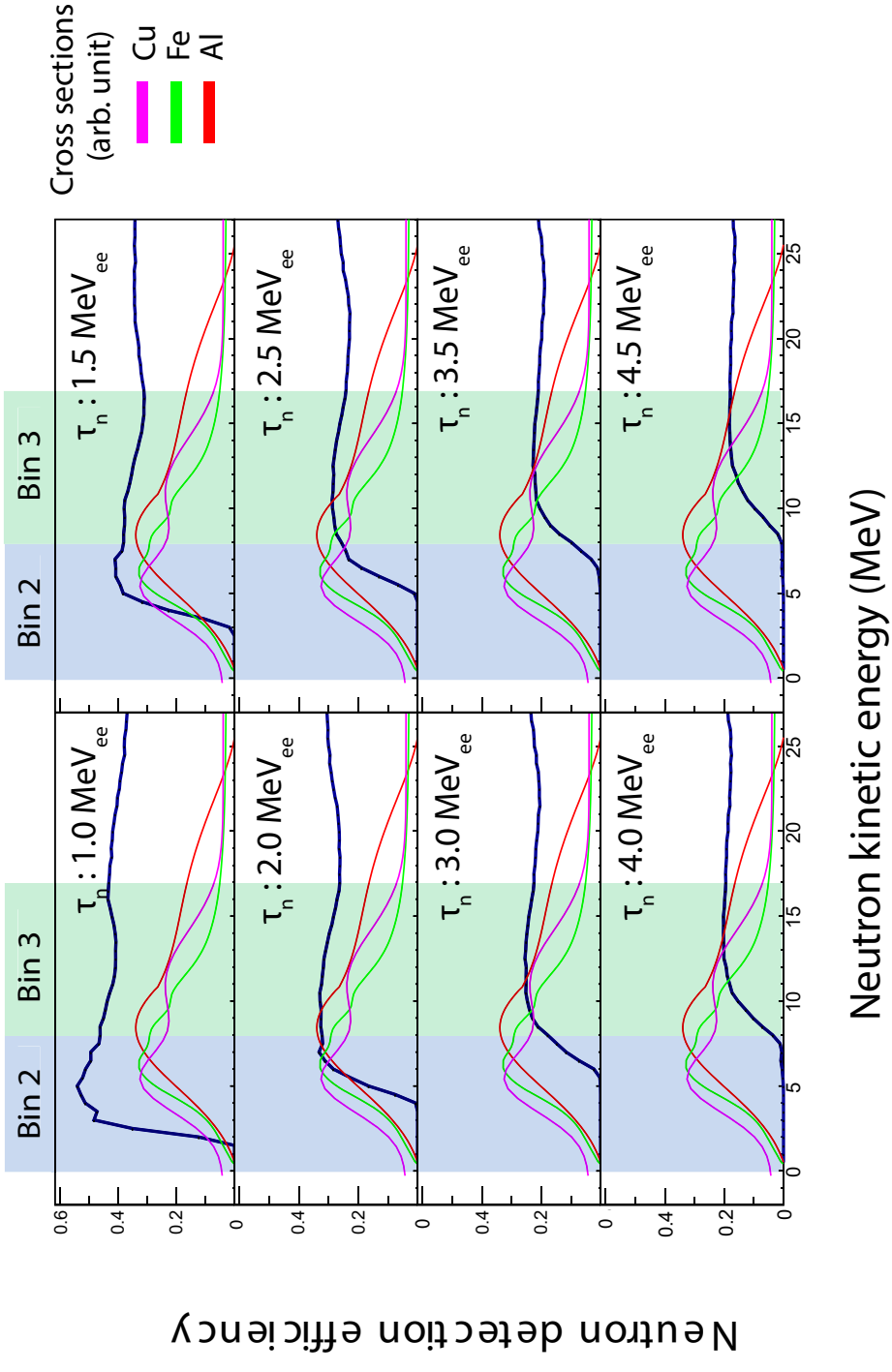

FIGURE E.3: The detection efficiency of the pentagonal Nordball detector for 8 different detector threshold settings together with overlaid photoknockout cross sections for ^{27}Al, ^{56}Fe and ^{63}Cu, in red, green and purple respectively. The neutron energies corresponding to photon-energy bins 2 (9.85 — 19.86 MeV) and 3 (19.86 — 29.05 MeV are shown as well. The simulated detection efficiency is the thick blue line. The threshold τ_n is set between 1.5 — 5.0 MeV$_{ee}$.

Appendix F

Photospectra from a Be-based Neutron Source

Goal

The goal of this effort was to investigate both the radiological conditions produced by the Be-based neutron source and the background at the Source Testing Facility.

Setup

The 1.5" × 1.5" cylindrical $LaBr_3$:Ce detector used to detect the gamma-rays is shown in Fig. F.1. A $LaBr_3$:Ce crystal of these dimensions is anticipated to have an energy resolution of about 3% at 662 keV [20]. $LaBr_3$:Ce has an internal activity from the de-excitation of ^{138}La via gamma-ray decay at an energy of 1.43 MeV [21] — a very useful self-calibration peak.

FIGURE F.1: The $LaBr_3$:Ce detector used in these measurements.

The detector was operated at +660 V generating a negative signal as shown in Fig. F.2. The signal was inverted and amplified before being passed to a MCA[1]. Data were analysed using the Maestro software from Ortec[2].

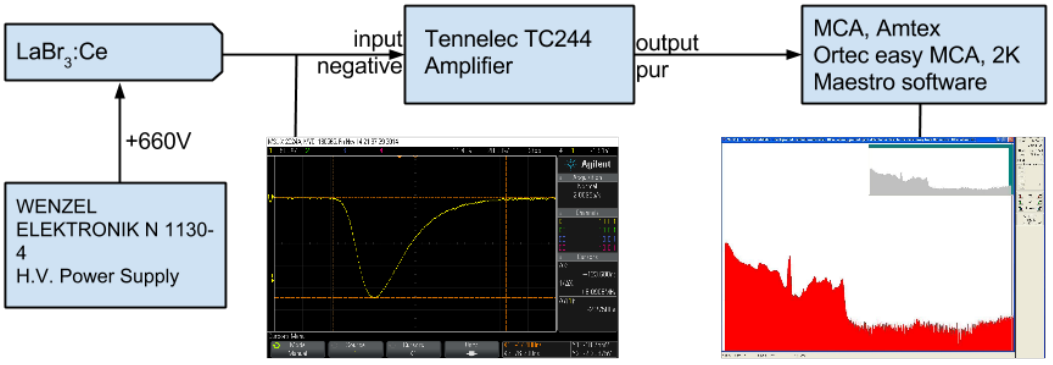

FIGURE F.2: An overview of the data acquisition and display.

Measurements

The detector was placed at different positions around the STF as shown in Fig. F.3, with increasing distance from and shielding against the source. Fig. F.4 shows the unshielded source measurement (A) as well as when a water jug was placed in between the source

[1]The multichannel analyser (MCA) used was an Amtex Ortec Easy MCA with 2048 channels.
[2]http://www.ortec-online.com/Solutions/applications-software.aspx.

and detector (B) resulting in a 2.22 MeV neutron-capture gamma-ray from the p(n,γ)d reaction.

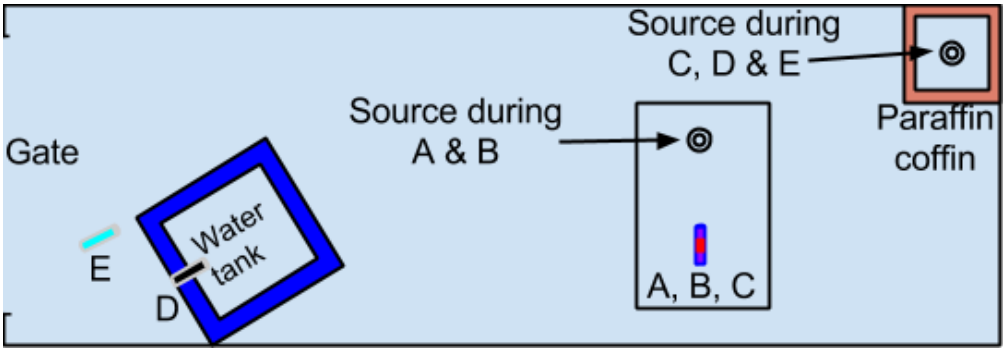

FIGURE F.3: The detector positions within the STF used for the measurements reported on here are marked A, B, C, D and E.

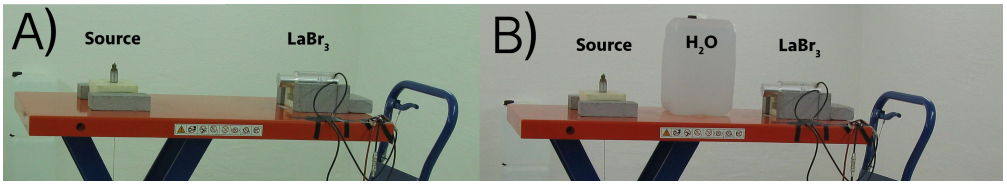

FIGURE F.4: Measurements A and B. The source is located on the left side of the table and the detector on the right. A) is a measurement without shielding. For B), a 20 cm thick jug of pure water was placed between source and detector.

For the other measurements, the source was located in the paraffin- and water-shielded coffin shown in Fig. F.5.

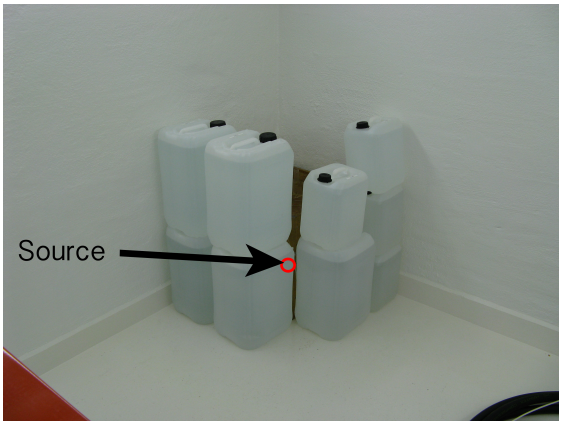

FIGURE F.5: The paraffin- and water-shielded source coffin used for the red, black and cyan colored measurements presented in Fig. F.6 and discussed below.

Apart from the 1.43 MeV self-calibration peak of the $LaBr_3$:Ce detector, peaks at 2.22 MeV (due to neutron capture by hydrogen in paraffin and water) and at 4.44 MeV (due to the de-excitation of the first excited state of $^{12}C^*$ following $^{9}Be(\alpha,n)^{12}C^*$ reaction) were anticipated [22].

Results

The results are presented in Fig. F.6.

- Purple, pos. A: Taken 0.5 m from the source with no shielding between the source and detector. Recall Fig. F.4 A).

- Blue, pos. B: Taken 0.5 m from the source with a 20 cm thick water jug between the source and detector. Recall Fig. F.4 B). A new peak has appeared at 2.22 MeV. This is the gamma-ray resulting from neutron capture on hydrogen [23].

- Red, pos. C: Taken with the $LaBr_3$:Ce detector placed 3 m from the source which was located in the coffin. Recall Fig. F.5. While the intensity of this distribution is weakened with respect to the blue distribution, the 4.44 MeV de-excitation gamma-ray and its corresponding escape peaks are still clearly visible.

- Black, pos. D: Taken 5 m from the source in the coffin with the $LaBr_3$:Ce detector in one of the detector penetrations of the water tank. Room-background peaks below the 1.43 MeV self-calibration peak have faded, as have the 4.44 MeV de-excitation gamma-ray and the corresponding escape peaks. But the 4.44 MeV gamma-ray and corresponding escape peaks are still clearly visible.

- Cyan, pos. E: Taken with the entire water tank as a shield between the source in the coffin and the $LaBr_3$:Ce detector. The 4.44 MeV gamma-ray and corresponding escape peaks are only barely visible.

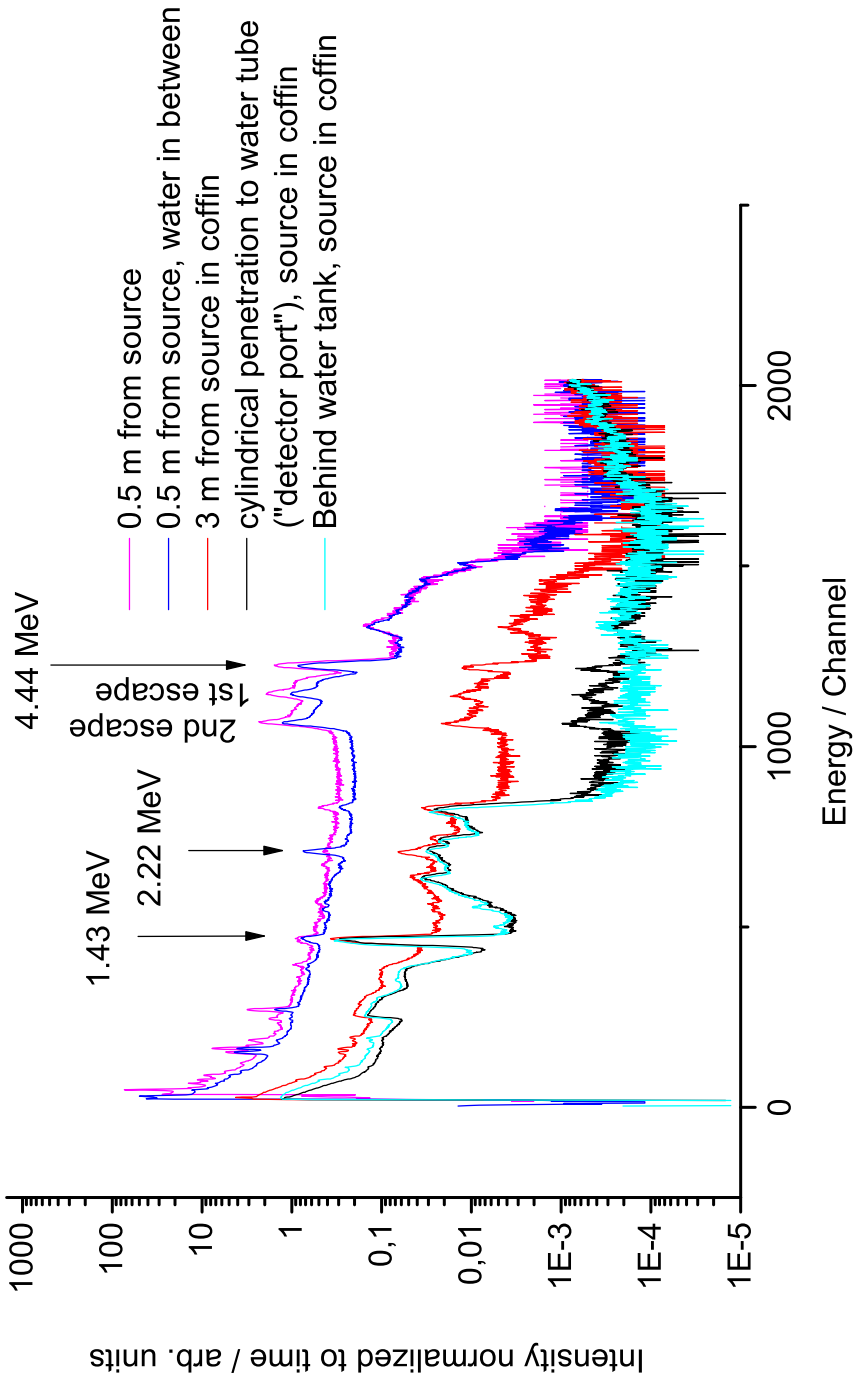

FIGURE F.6: Photospectra gathered with the $LaBr_3$:Ce detector located at different positions around the STF.

Conclusion

The results agree with expectations. The gamma-rays from the source and shielding are understood. The room background in the STF is low.

Acknowledgements

The author wishes to acknowledge P. Golubev for providing the detector, M. Ekholm for general setup help and M. Elfman for providing guidelines on radiation safety.

Appendix G

Constructing a ^{10}B Neutron Detector

A thermal-neutron detector was constructed based on the isotope ^{10}B and tested at the STF.

Principle of detection

The lack of charge of neutrons makes them difficult to detect directly. ^{10}B reacts with thermal neutrons and can thus be used as a converter of neutrons into charged particles that are more easily detected. ^{10}B has a large thermal neutron cross section for the reaction $^{10}\mathrm{B}(n,\alpha)^{7}\mathrm{Li}$. When a neutron is absorbed, an α-particle is instantaneously emitted. The α and recoiling ^{7}Li are produced at 180° from each other with two possible energy configurations corresponding to the branching ratios

$$\begin{aligned} \mathrm{n} + {}^{10}\mathrm{B} &\rightarrow \alpha(1.47\ \mathrm{MeV}) + {}^{7}\mathrm{Li}(0.84\ \mathrm{MeV}) \qquad \mathrm{BR} = 94\% \\ \mathrm{n} + {}^{10}\mathrm{B} &\rightarrow \alpha(1.78\ \mathrm{MeV}) + {}^{7}\mathrm{Li}(1.10\ \mathrm{MeV}) \qquad \mathrm{BR} = 6\%. \end{aligned} \tag{G.1}$$

Both the α and ^{7}Li deposit their kinetic energy in a gas mixture of $\mathrm{Ar/CO_2}$. They will travel in the gas creating ionization until they stop. The resulting free ionization electrons can be collected by applying a high voltage to a plane of wires, creating an electric field and attracting the electrons. This is how the detector registers a neutron event, by collecting ionization electrons. The more ionization electrons collected, the more energy the particle causing them had. The process is illustrated in Fig. G.1.

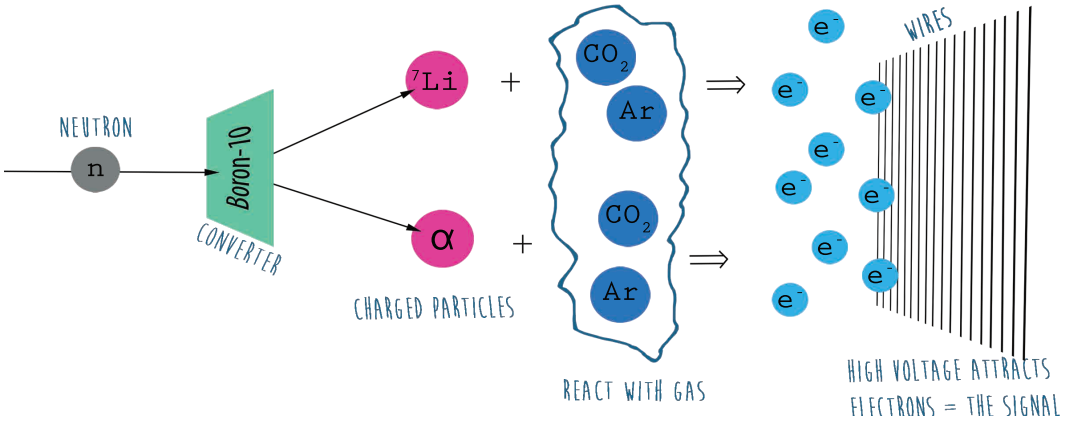

FIGURE G.1: The principle from incoming neutron to detected signal. The neutron reacts with ^{10}B resulting in ^{7}Li and an α-particle. The ^{7}Li and α deposit their energy in a gas of CO_2 and Ar. The resulting ionization electrons are collected by wires with a high voltage applied to them. The number of ionization electrons collected is proportional to the energy of the charged particles.

Construction

The housing of the detector was milled by SvedalaMek (http://www.svemek.com/). It measures 12 × 20 × 23 cm^3 and can hold five different wire planes with separate connectors. Above and below each wire plane, plates coated with different thicknesses (between 0.3 — 3 μm) of ^{10}B are placed. The ^{10}B plates are grounded and the wire plane connectors are attached to high voltage. The housing has penetrations for gas. The gas penetrations were equipped with quick connectors to make reconfiguring the detector straightforward, see the left panel of Fig. G.6. The detector operates at 1 atm pressure. All connectors and the opening hatch were carefully sealed with generically branded, natural buna rubber o-rings. The wires used to collect the ionization electrons are thin (20 — 50 μm) gold-plated tungsten. In order to construct the wire planes, each with 20 of these fragile wires spaced by 3 mm and uniformly tensioned, a wiring frame was constructed, see Fig. G.2. The wiring frame maintained an even tension in the wire using a counterweight filled with 1.2 liters of water for the 20 μm wire. With two wire planes mounted on the rotatable part of the wiring frame (marked C in Fig. G.2), the wire rolled out to the correct position for each rotation of the device. The rotation occured on an M6 thread, making it move 1 mm sideways for each rotation. Once the entire wire frame was finished, the wires to be kept (every third wire for 3 mm spacing) were soldered onto the wire plane. Excess wire was removed and a new set of wire planes could then be mounted. A finished wire plane with 3 mm spacing between the wires is shown in Fig. G.3. All the wires of a wire plane receive the same voltage. If all the wires were 20 μm thick, the electric field at the edges of the plane would be too strong, risking electric sparks and breakdowns of the detector. The electric field at the surface

of a wire is proportional to 1/R, where R is the wire radius. With 50 μm wires at the edges, the electric field is lowered and the risk of breakdown is greatly reduced.

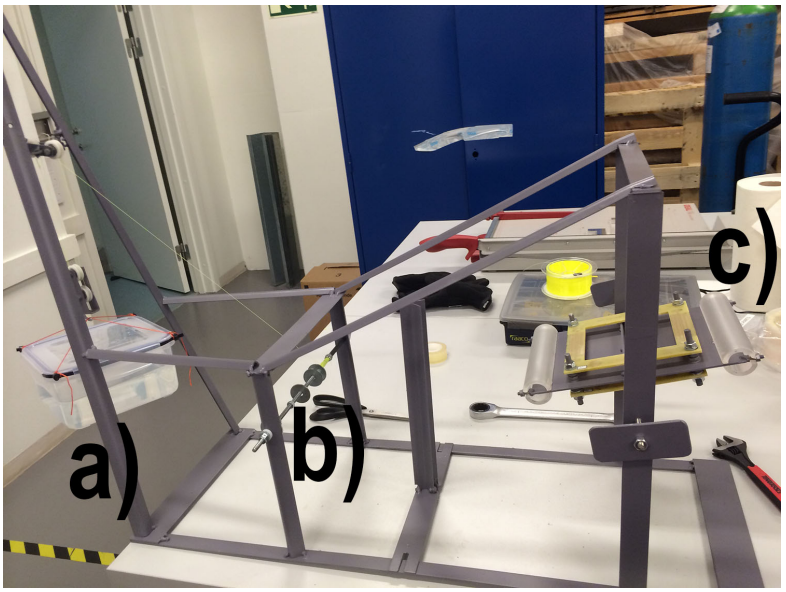

FIGURE G.2: The wiring frame used to place wires on the wire planes. **a)** the counterweight setting the tension of the wires. **b)** the wire roll **c)** wire-plane holder which is rotated by hand moving 1 mm away from the perspective of the camera for each rotation.

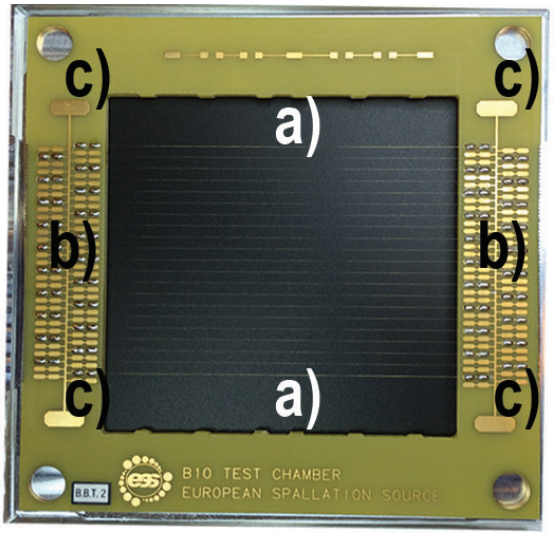

FIGURE G.3: A wire plane with 3 mm spacing between the 20 μm wires. The corner holes are used for attaching the plane to the detector. The top and bottom wires **a)** are 50 μm thick. All the wires are soldered in place on the metal connectors, **b)**. High voltage is applied to one of the contacts **c)** which is also where the signal is collected.

In order to channel the neutrons from the source to the wireplanes without interacting with the rest of the detector, a neutron "shield" was made. Gadolinium has a large neutron interaction cross section. Gadolinium powder was mixed with latex and cast

to cover the front and sides of the detector, see Fig. G.4. A neutron window was left unshielded, behind which the wire planes were mounted. The opposite side of the neutron window is shown in Fig. G.5. Wire frames were attached in the detector, alternated with ^{10}B-coated plates below and above. The ^{10}B plates were connected to the body of the detector as ground. The wire planes were connected via feed-throughs to the outside of the detector. The feed-throughs supply the high voltage to the wires and collect the signal. Each wire frame was connected to a seperate feed-through.

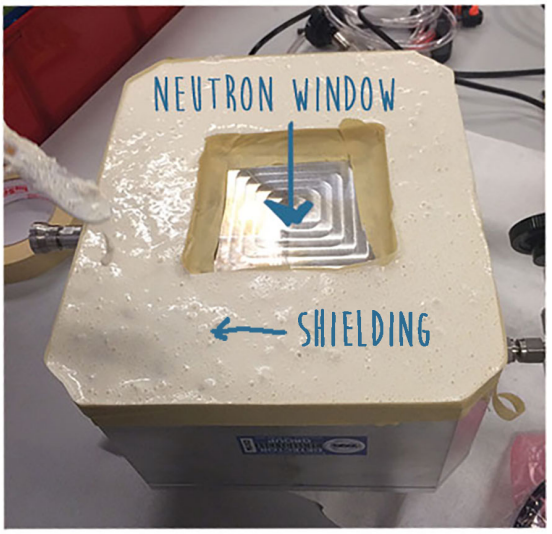

FIGURE G.4: Molding of shielding for the detector container with a mixture of gadolinium and latex. A window is left unshielded in front of the wire planes.

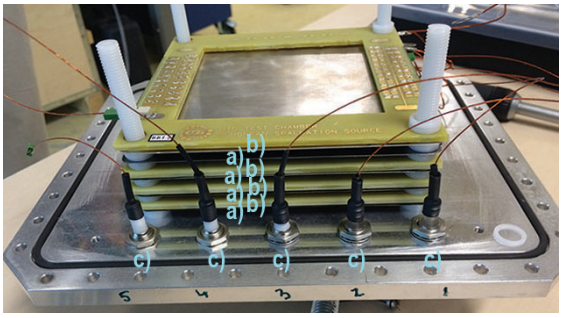

FIGURE G.5: The wire planes, **a)**, and ^{10}B coated plates, **b)** are layered with ^{10}B on both sides of each wire plane. The ^{10}B plates are connected to the metal base as ground. The 5 wire planes are connected to the 5 feed-throughs, **c)**, to the outside of the detector.

The detector was sealed with a long o-ring and 22 M4-threaded screws. Once sealed, the gas connectors were attached and shielding was placed around the front and sides of the detector. In Fig. G.6, the closing procedure and the finished shielded detector are shown.

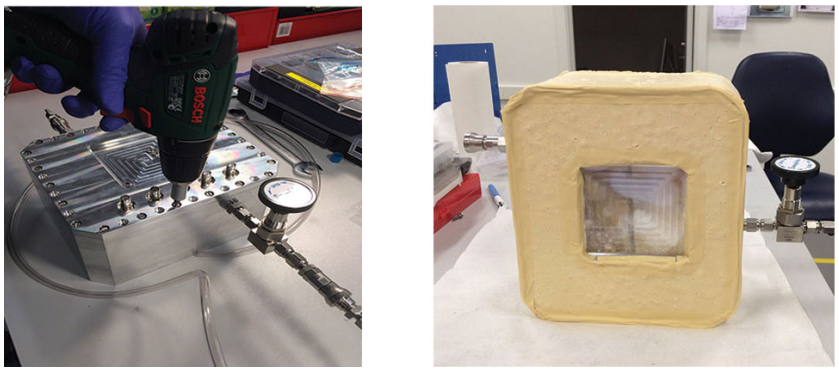

FIGURE G.6: **Left:** The detector is closed with 22 M4 screws. The gas input valve is seen in the lower right. The gas output valve is seen on the upper left of the detector. **Right:** A picture from the front of the assembled detector. The gadolinium-latex shielding covers the front and sides, apart from the neutron window in the center. Ar/CO_2 gas flow can be fine-tuned via the valve on the right.

Testing

For testing, the detector was taken to the Source-Testing Facility (STF). STF is a detector-testing facility located in the Micro Hall at the Fysicum at Lund University. Here, a beryllium-based neutron source can be used together with different shielding options for neutron-detection testing. The beryllium-based source was used to irradiate the detector with neutrons between 2 MeV to 11 MeV. From an ISEG high voltage supply, 1000 V was applied to a preamplifier (ORTEC 192PC) to both supply the high voltage to the detector and read the signal from it, see Fig. G.7. Signals were passed to an amplifier for shaping and to multi-channel analyzer (MCA8000D) connected to a PC via USB to be counted and plotted using the Amptek DPPMCA software.

A typical plot from a 500 s run is shown in Fig. G.8. As expected from Eq. G.1, the 0.84 MeV ^{7}Li and 1.47 MeV α clearly dominate. The less common 1.78 MeV α-particles were also observed. The 1.10 MeV ^{7}Li peak shows up as a shoulder on the larger 0.84 MeV peak.

Presentation

For the presentation of this project, a poster was made describing the principle behind ^{10}B neutron detection, the major steps of building the detector and a typical output from testing at the STF, see Fig. G.9.

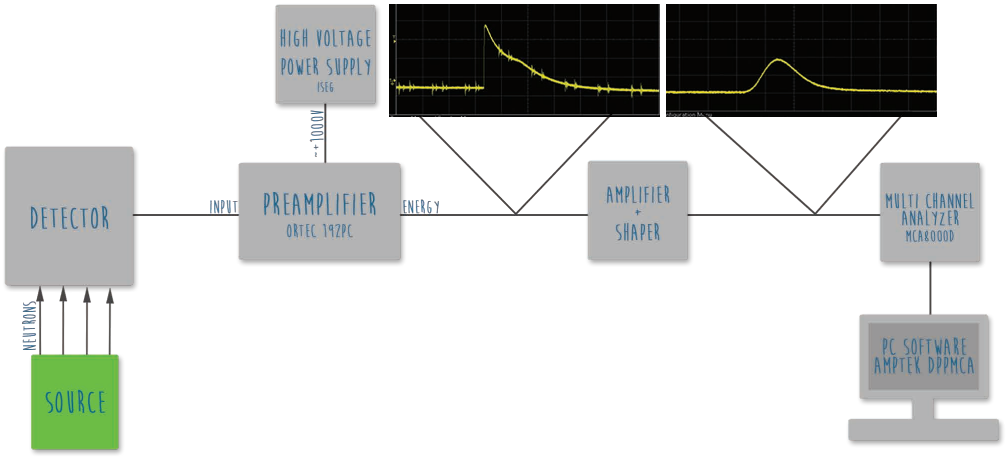

FIGURE G.7: Scheme of the electronics used for the testing of the detector. The preamplifier supplied the detector with high voltage from the power supply. Neutrons from the source created a signal in the detector which was passed to the amplifier for shaping. Inset images of the signal before and after shaping and amplification were taken with an Agilent Technologies MSO-X 2024A oscilloscope. The signals were counted in the multi-channel analyzer which was connected to a PC via USB.

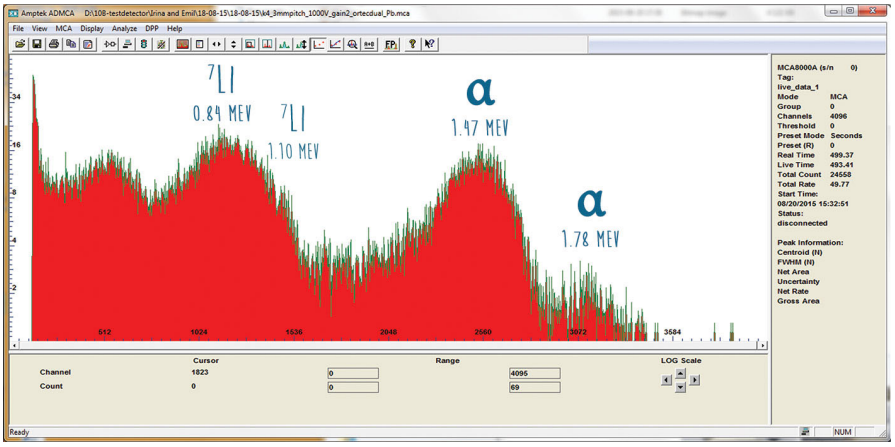

FIGURE G.8: Typical output from a 500 s measurement using the PC software AMPTEK DPPMCA. The 0.84 MeV ^{7}Li and 1.47 MeV α dominate the spectra. The less common 1.10 MeV ^{7}Li and 1.78 MeV α are also observed. 1.10 MeV ^{7}Li appears as a shoulder on the 0.84 MeV peak.

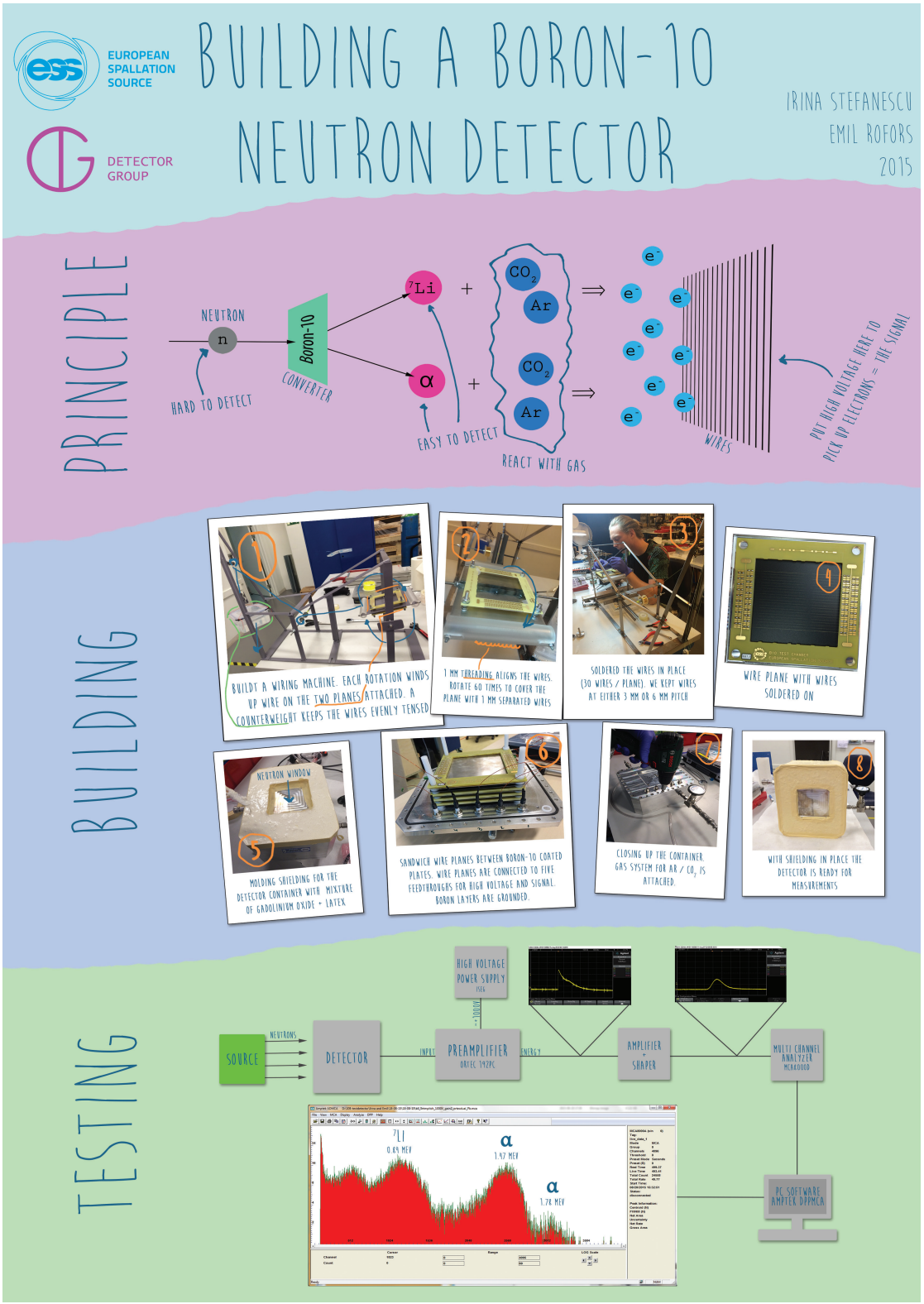

FIGURE G.9: A poster presenting the project, now hanging on the wall of STF. It is divided into three phases: principle of ^{10}B neutron detection, building of the detector and testing in the STF.

Bibliography

[1] Nuclear Stability and Magic Numbers - Chemwiki. URL http://chemwiki.ucdavis.edu/Core/Physical_Chemistry/Nuclear_Chemistry/Nuclear_Stability_and_Magic_Numbers.

[2] K Nakamura and Group Particle Data. Review of Particle Physics. Journal of Physics G: Nuclear and Particle Physics, 37(7A):75021, 2010. ISSN 1674-1137. doi: 10.1088/1674-1137/38/9/090001. URL http://stacks.iop.org/0954-3899/37/i=7A/a=075021.

[3] Seyed Amir Feghhi, Zohreh Gholamzadeh, and Claudio Tenreiro. Investigation of the optimal material type and dimension for spallation targets using simulation methods. Journal of Theoretical and Applied Physics, 8(1):1, 2014. ISSN 2251-7235. doi: 10.1186/2251-7235-8-1. URL http://www.jtaphys.com/content/8/1/1.

[4] H. Weile, L. Van der Zwan, and K. W. Geiger. The neutron continuum from the9Be+α reaction. Zeitschrift für Physik, 259(3):275–284, jun 1973. ISSN 0044-3328. doi: 10.1007/BF01408069. URL http://link.springer.com/10.1007/BF01408069.

[5] Am-Be-Source Spectrum - Gamma spectroscopy - Wikipedia. URL https://en.wikipedia.org/wiki/Gamma{_}spectroscopy{#}/media/File:Am-Be-SourceSpectrum.jpg.

[6] Earl K. Hyde. NATURAL RADIOACTIVITY OF THE HEAVY ELEMENTS: A COMPREHENSIVE REVIEW. 1963. URL https://publications.lbl.gov/islandora/object/ir{%}3A137656/.

[7] J.H. NEILER and P.R. BELL. Alpha-, Beta- and Gamma-Ray Spectroscopy. Elsevier, 1968. ISBN 9780720400830. doi: 10.1016/B978-0-7204-0083-0.50010-9. URL http://www.sciencedirect.com/science/article/pii/B9780720400830500109.

[8] Björn Nilsson. High-Resolution Measurement of the 4He(gamma,n) Reaction in the Giant Resonance Region. 2003.

[9] K. F. Flynn. . Nuclear Instruments and Methods in Physics Research, 27(13), 1964.

[10] H. H. Knox and T. G. Miller. . Physics Research, 101, 519.

[11] S Agostinelli, J Allison, and K Amako. Geant4-a simulation toolkit. Nuclear Instruments and Methods in Physics Research A, 506:250–303, 2003. ISSN 01689002. doi: 10.1016/S0168-9002(03)01368-8. URL http://ns1.hep.scitec.kobe-u.ac.jp/{~}kurasige/Geant4/GeneralPaper-NIM.pdf$\delimiter"026E30F$npapers3://publication/uuid/CD0D7D13-0546-4B05-84BF-5AA09FD06966.

[12] Julius Scherzinger. Private communications. 2015.

[13] CAEN Tools for Discovery. 2016. URL http://www.caen.it/.

[14] Teledyne LeCroy. 2016. URL http://teledynelecroy.com/.

[15] N. R. Stanton. Monte Carlo Program for Calculating Neutron Detection Efficiencies in Plastic Scintillator. URL https://www.ntis.gov/Search/Home/titleDetail/?abbr=COO154592.

[16] R a Cecil, B D Anderson, and R Madey. Improved predictions of neutron detection efficiency. Nuclear Instruments and Meathods, 161(3):439–447, 1979. ISSN 0029-554X. doi: http://dx.doi.org/10.1016/0029-554X(79)90417-8. URL http://shop-pdp.net/efhtml/article.htm.

[17] Photonuclear IAEA-CRP. URL https://www-nds.iaea.org/photonuclear/.

[18] Laurie S. Waters, Gregg W. McKinney, Joe W. Durkee, Michael L. Fensin, John S. Hendricks, Michael R. James, Russell C. Johns, and Denise B. Pelowitz. The MCNPX Monte Carlo radiation transport code. AIP Conference Proceedings, 896 (May 2014):81–90, 2007. ISSN 0094243X. doi: 10.1063/1.2720459. URL http://scitation.aip.org/content/aip/proceeding/aipcp/10.1063/1.2720459.

[19] K. G. Fissum. Inclusive Photoproduction of Positive Pions. SAL Report No. 46, 1993.

[20] E. V. D. van Loef, P. Dorenbos, C. W. E. van Eijk, K. Krämer, and H. U. Güdel. High-energy-resolution scintillator: Ce[sup 3+] activated LaBr[sub 3]. Applied Physics Letters, 79(10):1573, 2001. ISSN 00036951. doi: 10.1063/1.1385342. URL http://scitation.aip.org/content/aip/journal/apl/79/10/10.1063/1.1385342.

[21] Peter R. Menge, G. Gautier, A. Iltis, C. Rozsa, and V. Solovyev. Performance of large lanthanum bromide scintillators. Nuclear Instruments and

Methods in Physics Research Section A: Accelerators, Spectrometers, Detectors and Associated Equipment, 579(1):6–10, 2007. ISSN 01689002. doi: 10.1016/j.nima.2007.04.002. URL http://www.sciencedirect.com/science/article/pii/S0168900207005591.

[22] Héctor René Vega-Carrillo, Eduardo Manzanares-Acuña, Ana Maria Becerra-Ferreiro, and Aureliano Carrillo-Nuñez. Neutron and gamma-ray spectra of 239PuBe and 241AmBe. Applied Radiation and Isotopes, 57(2):167–170, 2002. ISSN 09698043. doi: 10.1016/S0969-8043(02)00083-0. URL http://www.sciencedirect.com/science/article/pii/S0969804302000830.

[23] R.C. Greenwood and W.W. Black. The binding energy of the deuteron determined from measurement of the hydrogen neutron capture gamma-ray energy. Physics Letters, 21(6):702–704, 1966. ISSN 00319163. doi: 10.1016/0031-9163(66)90133-8. URL http://www.sciencedirect.com/science/article/pii/0031916366901338.

The project reported upon in this thesis
was performed in collaboration with

The Source-based Neutron Irradiation Group
of the Division of Nuclear Physics at Lund University

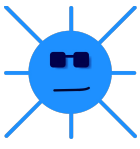

The Detector Group of the European Spallation Source

and

The Neutron Optics and Shielding Group of the
European Spallation Source